

1 **Revealing Hidden Oxygen Variability in the North Pacific: A Two-**
2 **Decade Analysis Using GOBAI-O₂**

3
4

5 Miho Ishizu^{1,2}, Tomomichi Ogata³

6

7 *¹Center for Climate Physics, Institute for Basic Science, Busan 46241, Republic of Korea*

8 *²Pusan National University, Tonghapgigyegwan Bldg 2 Busandaehak-ro, 63 beon-gil, Geumjeong-gu,*
9 *Busan 46241, Republic of Korea*

10 *³Japan Agency for Marine-Earth Science and Technology, Environmental Variability Prediction and*
11 *Application Research Group, Yokohama Institute for Earth Sciences, 3173-25 Showa-machi,*
12 *Kanagawa-ku, Yokohama 236-0001, Japan*

13 To whom correspondence may be addressed. Email: mishizu@pusan.ac.kr

14

15

16 **Abstract**

17 Oceanic dissolved oxygen concentrations are thought to be declining under ongoing global warming,
18 yet their variability remains less well understood than that of physical parameters such as temperature
19 and salinity, primarily due to the limited spatial and temporal coverage of oxygen observation. Here,
20 we examine linear trends in potential temperature, salinity, and dissolved oxygen in the North Pacific
21 over the past two decades (2004–2023), using the GOBAI-O₂ dataset. We compare the diagnosed
22 oxygen trends with those of physical parameters to reveal the spatial structure of recent changes. The
23 oxygen trends inferred from GOBAI-O₂ are broadly consistent with trends observed along ship-based
24 hydrographic repeat lines. While basin-scale deoxygenation is evident, we also identify localized
25 oxygen increases on specific density surfaces. By relating these patterns to the surrounding physical

26 environment, we find that the spatial heterogeneity in oxygen trends is consistent with known
27 oceanographic processes, including the southward retreat of the oxygen minimum layer and the
28 northward migration of a front separating the subtropical and subarctic gyres. These results underscore
29 the value of GOBAI-O₂ data in linking physical variability to previously unrecognized biological and
30 biogeochemical patterns in the ocean.

31

32

33 **Plain Language Summary**

34 1. We investigated how potential temperature, salinity, and dissolved oxygen have changed in the
35 North Pacific over the past 20 years using GOBAI-O₂ dataset, and we examined the physical
36 processes responsible for these trends.

37 2. The trends identified in this study are broadly consistent with findings from previous research, and
38 improved spatial coverage of GOBAI-O₂ allowed us to reveal connections between regional
39 patterns that we previously only partially understood.

40 3. Overall, dissolved oxygen decreased across much of the North Pacific. However, some regions
41 showed increasing oxygen levels, indicating that the changes were not uniform. These non-uniform
42 patterns reflect known physical ocean processes. For example, higher oxygen levels in the northern
43 North Pacific are consistent with a northward shift of the front separating the subtropical and
44 subarctic gyres. In the equatorial Pacific, the reduced westward extent of the oxygen minimum
45 layer corresponds to a weakening and poleward shift of the North Equatorial Countercurrent
46 (NECC) on interdecadal timescales.

47 4. These findings provide new evidence that links large-scale physical ocean changes to previously
48 unclear changes in biological and biogeochemical observations.

49

50 Keywords: dissolved oxygen, 20-year linear trends, Bio-Argo float data, global warming

51

52 **1. Introduction**

53 Over recent decades, the global ocean has experienced a decline in its dissolved oxygen inventory, a
54 trend projected to continue through the 21st century [Keeling et al., 2010; Breitburg et al., 2018;
55 Stramma and Schmidtko, 2021; Limburg et al., 2020; Ito et al., 2017, 2024; Kolodziejczyk et al., 2024].

56 This deoxygenation is driven in part by reduced ocean oxygen solubility under rising sea-surface
57 temperatures, which promotes oxygen outgassing. In addition, enhanced stratification and a slowdown
58 of ocean circulation under global warming can reduce interior ventilation and oxygen supply [Keeling
59 et al., 2010, Bopp et al. 2013; Ito et al. 2017]. Ocean oxygen loss can negatively affect aerobic marine
60 organisms [Pörtner and Farrell, 2008; Sampaio et al., 2021], alter biogeochemical cycles, and
61 potentially induce climate-relevant feedback [Berman-Frank et al., 2008]. Historical deoxygenation
62 has been inferred from globally distributed observations [Helm et al., 2011; Schmidtko et al., 2017;
63 Ito et al., 2017; Takatani et al., 2012; Sasano et al., 2015; Lauvset et al., 2022b], and Earth system
64 models have been used to simulate both historical and future changes in ocean oxygen [Bopp et al.,
65 2013; Kwiatkowski et al., 2020; Li et al. 2020].

66

67 Observed oxygen trends have traditionally been assessed using the discrete measurements of dissolved
68 oxygen concentration (O_2), typically obtained by Winkler titration [Winkler, 1988]. These
69 measurements are also used to calibrate electrode- and more recently, optode-based oxygen sensors
70 mounted on conductivity-temperature-depth (CTD) profilers [Helm et al. 2011; Schmidtko et al.,
71 2017; Lauvset et al., 2022b]. Although programs such as WOCE, CLIVAR, and GO-SHIP have
72 collected high-quality oxygen measurements globally, repeat occupation intervals are commonly on
73 the order of a decade, limiting the ability to robustly quantify annual to seasonal variability. Higher-

74 frequency ship-based observations exist in a few regions [Takatani et al. 2012; Sasano et al., 2015],
75 but their spatial coverage is limited. Consequently, despite attempts to characterize basin-scale pattern
76 [Ito et al. 2017; Stramma et al. 2020; Kolodziejczyk et al. 2024], observational constraints have
77 hampered a spatially and temporally comprehensive understanding of dissolved oxygen variability and
78 trends.

79

80 Oxygen sensors were first deployed on Argo profiling floats in the mid-2000s. Since then,
81 approximately 1,800 oxygen-equipped floats have been deployed worldwide, substantially advancing
82 the observational basis for assessing oxygen variability and trends [Sharp et al., 2023]. The expansion
83 toward a global biogeochemical (BGC) Argo network has improved sampling in regions that were
84 previously sparsely observed [Claustre et al., 2020]. In parallel, major progress has been made in
85 calibration, adjustments, and quality control of oxygen measurements, including pre-deployment drift
86 corrections [D'Asaro and McNeil, 2013; Johnson et al., 2015; Bittig and Körtzinger, 2015; Bushinsky
87 et al., 2016; Drucker and Riser, 2016; Nicholson and Feen, 2017], climatology-based calibrations
88 [Takeshita et al., 2013], in-air oxygen measurement calibrations [Körtzinger et al., 2005; Bittig and
89 Körtzinger, 2015; Johnson et al., 2015; Bushinsky et al., 2016], post-deployment drift corrections
90 [Johnson et al., 2017; Bittig et al., 2018a, b], and the standardized delayed-mode quality control
91 procedures [Maurer et al., 2021]. Together, these developments have reduced uncertainty and
92 improved the consistency of optode-based [O₂] measurements from Argo floats.

93

94 To date, oxygen observations from Argo floats have been used primarily in regional process studies,
95 including air-sea oxygen exchange [Wolf et al., 2018], upper-ocean primary production [Alkire et al.,
96 2012; Estapa et al., 2019], biological pump efficiency [Johnson and Bif, 2021], and the dynamics of
97 the oxygen minimum zone [Udaya Bhaskar et al., 2021]. Recently, Sharp et al. [2023] produced a

98 four-dimensional gridded [O₂] product, GOBAI-O₂ (Gridded Ocean Biogeochemistry from Artificial
99 Intelligence (AI) – Oxygen). GOBAI-O₂ is constructed using machine-learning methods trained on
100 oxygen observations and designed to reconstruct spatial patterns, seasonal cycles, and decadal
101 variability, particularly in regions where observational data gaps coincide with high background O₂
102 variability.

103

104 In the North Pacific, several studies have documented heterogeneous oxygen trends. Using an
105 objectively mapped monthly climatology of O₂ based on the World Ocean Database 2013 (WOD13)
106 [Boyer et al. 2013], Ito et al. [2017] reported multidecadal variability and trends in dissolved O₂ in
107 the surface-layer oxygen from 1958 to 2013. Sasano et al. [2015], using the high-frequency shipboard
108 sections along the 137°E and 165°E lines from 1987 to 2011, reported oxygen declines in the northern
109 subtropical to subtropical-subarctic transition zones of $-0.45 \pm 0.16 \mu\text{mol/kg/yr}$ at 25.3 σ_θ and $-0.45 \pm$
110 $0.14 \mu\text{mol/kg/yr}$ at 26.8 σ_θ , respectively. They also identified a significant oxygen increase in the
111 tropical Oxygen Minimum Layer (OML) of $+0.36 \pm 0.004 \mu\text{mol/kg/yr}$, highlighting pronounced spatial
112 heterogeneity. At broader scales, Stramma et al. [2020] analyzed historical bottle data and reported
113 links between oxygen variability and climate modes such as the Pacific Decadal Oscillation (PDO)
114 and the North Pacific Gyre Oscillation (NPGO), although sparse sampling makes it difficult to robustly
115 connect regional trends to physical mechanisms. Collectively, previous studies indicate that oxygen
116 changes in the North Pacific can be strong, spatially non-uniform, and potentially driven by both
117 circulation/ventilation changes and biologically mediated oxygen consumption [Sasano et al. 2015;
118 2018; Ito et al. 2017; 2024; Stramma et al., 2020; Kolodziejczyk et al. 2024].

119

120 Because observational opportunities to quantify trends in dissolved oxygen—together with concomitant
121 changes in temperature and salinity—remain limited, gridded products such as GOBAI-O₂ are
122 becoming increasingly valuable for basin-scale analyses. In this study, we use GOBAI-O₂ to quantify

123 linear trends in potential temperature, salinity, and dissolved oxygen in the North Pacific over 2004–
124 2023 and examine how their trends are connected in both depth and density space. We further discuss
125 the extent to which the diagnosed oxygen trends can be interpreted in terms of physical drivers,
126 including surface warming, stratification changes, and circulation variability in the North Pacific.

127

128 **2. Data and Methods**

129 **2.1 GOBAI-O₂ dataset**

130 We use GOBAI-O₂, a four-dimensional, monthly gridded product of dissolved oxygen (O₂) in the
131 ocean interior, generated using machine learning (ML) algorithms trained on both Argo float oxygen
132 measurements and ship-based discrete observations [Sharp et al., 2023]. GOBAI-O₂ is mapped onto
133 the temperature- salinity fields provided by the global Argo array [Roemmich and Gilson, 2009]. The
134 underlying oxygen training database combines ship-based measurements from GLODAPv2.2022 and
135 Argo float data distributed through the Argo Global Data Assembly Centers, after quality control
136 [Sharp et al., 2023] (<https://doi.org/10.25921/z72m-yz67>).

137

138 The ML models predict O₂ using predictors that include absolute salinity, conservative temperature,
139 potential density anomaly, hydrostatic pressure, bottom depth, and additional spatiotemporal
140 covariates representing geographic, seasonal, and interannual variability. Biological processes are not
141 explicitly parameterized in the ML framework; however spatiotemporal covariates can implicitly
142 capture biological influences to some extent [Giglio et al., 2018].

143

144 GOBAI-O₂ is produced using two ML approaches: feed-forward networks (FNNs) and random forest
145 regression (RFRs, [Breiman, 2001]). The final O₂ estimate at each grid point is taken as the mean
146 of the FNN and RFR predictions. The dataset spans 2004–2023 at monthly resolution on a 1° × 1°

147 latitude–longitude grid, covering 86% of the global ocean area. The product is provided on 58 vertical
148 levels from the surface to ~2,000 m. Sharp et al. [2023] reported $0.79 \pm 0.04\%$ per decade decrease
149 in the oxygen inventory of the upper 2000 m over 2004–2022. Full details of their data sources,
150 processing, algorithm training, evaluation, and uncertainty estimation are given in Sharp et al. [2023].

151

152 2.2 Uncertainty estimates

153 GOBAI-O₂ provides an uncertainty estimate for each gridded O₂ value, constructed by combining
154 independent uncertainty components in quadrature [Sharp et al., 2023]:

$$155 \quad u([O_2])_{tot.} = \sqrt{u([O_2])_{meas.}^2 + u([O_2])_{grid.}^2 + u([O_2])_{alg.}^2} \quad (1),$$

156 where $u([O_2])_{meas.}^2$ represents measurement uncertainty of the underlying observations,
157 $u([O_2])_{grid.}^2$ is the gridding uncertainty associated with representing a four-dimensional
158 spatiotemporal volume by a single value, and $u([O_2])_{alg.}^2$ is the algorithmic uncertainty arising from
159 the ML estimation. We use $u([O_2])_{tot.}$ to characterize uncertainty in O₂ and to propagate uncertainty
160 into our oxygen trend estimates (Figs. 1–4). In most figures, we incorporate the mean uncertainty when
161 estimating linear O₂ trends.

162

163 2.3 Vertical grid and interpolation for isopycnal analysis

164 GOBAI-O₂ is provided on a $1^\circ \times 1^\circ$ horizontal grid with 58 depth levels: 2.5, 10, 30, 40, 50, 60, 70,
165 80, 90, 100, 110, 120, 130, 140, 150, 160, 170, 182.5, 200, 220, 240, 260, 280, 300, 320, 340, 360,
166 380, 400, 420, 440, 462.5, 500, 550, 600, 650, 700, 750, 800, 850, 900, 950, 1000, 1050, 1100, 1150,
167 1200, 1250, 1300, 1350, 1412.5, 1500, 1600, 1700, 1800, 1900 and 1975 m. The enhanced near-surface
168 vertical resolution is important for resolving strong gradients in temperature, salinity, density, and
169 oxygen within the mixed layer [Kara et al., 2000].

170

171 For analysis performed in density space, we interpolate the original depth-level data to 1-m vertical
172 grid using cubic spline interpolation and then evaluate linear trends on a $1^\circ \times 1^\circ \times 1$ m grid. This
173 approach enables computation of trends as a function of latitude (1° bins) and potential density
174 anomaly ($0.1\sigma_\theta$ bins) (Figs. 4–7). To evaluate sensitivity to interpolation choices, we repeated the
175 analysis using linear, shape-preserving cubic (PCHIP) interpolation and using coarser vertical grids
176 (2m and 5m). The resulting trend patterns show no material differences among interpolation methods
177 (Figs. S1 (a, b) and S2 (a, b)). The 5-m grid cannot resolve densities lighter than $24.0\sigma_\theta$ at some
178 latitudes; however, the main features are preserved across all tested resolutions.

179

180 **2.4 OFES model output**

181 In Section 3.3.2, we additionally use output from the eddy-resolving OGCM for the Earth Simulator
182 (OFES) [Masumoto et al., 2004; 2010; Sasaki et al., 2008] to examine the physical context of the
183 diagnosed variability. OFES is based on the MOM3 [Pacanowski and Griffies, 2000] and uses a quasi-
184 global domain spanning 75° S– 75° N with $0.1^\circ \times 0.1^\circ$ horizontal resolution and 54 vertical levels. The
185 model was initialized from rest using the World Ocean Atlas 1998 (WOA98) [Boyer and Levitus,
186 1997], and spun up for 50 years using climatological forcing derived from NCEP-NCAR reanalysis
187 [Kalnay et al., 1996]. After spin-up, a hindcast experiment was conducted from 1950 to 2024 using
188 daily NCEP-NCAR forcing. Here we analyze OFES output over 1950–2023.

189

190 **3. Results**

191 **3.1 Horizontal distributions of linear trends**

192 Figure 1 illustrates the horizontal and vertical distributions of linear trends in potential temperature,
193 salinity, and dissolved oxygen (O_2), over 2004–2023. Positive trends in potential temperature are

194 primarily confined to the surface layer above 200 m depth (Fig. 1a–c), with larger magnitudes at
195 higher latitudes. In contrast, negative trends emerge below the surface in the eastern tropical area
196 (180° – 120° W, 5° – 15° N) (Fig. 1b), extending westward and deepening with increasing depth (Fig.
197 1d–f). Below \sim 400 m, the spatial distributions of positive and negative temperature trends differ
198 between the subarctic and subtropical gyres.

199

200 Salinity trends exhibit generally negative values throughout the surface layer (Fig. 1h–i), consistent
201 with freshening. Localized positive salinity trends are detected in the Kuroshio–Oyashio transition
202 area and the northwest Pacific (140° – 180° E, 20° – 50° N), as well as in the tropical region (120° –
203 170° E, 0° – 10° N). Additional positive trends appear along the eastern boundary off California (130° –
204 199° W, 20° – 40° N). Below 200 m depth, salinity trends are weaker and broadly mirror the temperature
205 ones (Fig. 1j–k). Notably, negative salinity trends are evident around the Alaska gyre (170° – 130° W,
206 40° – 55° N) (Fig. 1j–l), a pattern that differs from the corresponding temperature trends.

207

208 Negative trends in dissolved O_2 are widespread across the North Pacific and extend throughout much
209 of the water column (Fig. 1o–u). Large negative trends are concentrated at higher latitudes near the
210 surface, with their locations shifting systematically with depth. Particularly strong O_2 declines are
211 observed along the northeastern boundary (140° – 130° W, 40° – 50° N) and within the southern
212 subtropical region (10° – 25° N) on density surfaces between 25.2 and $26.8\sigma_{\theta}$, corresponding to depths
213 of approximately 200–600 m (Fig. 1q–s). In contrast, weak positive O_2 trends are detected below 200
214 m depth in the Kuroshio–Oyashio transition zone (130° – 150° E, 30° – 40° N), extending into deeper
215 layers and spreading northeastward across the basin (Fig. 1r–u).

216

217 Positive O_2 trends are restricted to specific regions and depths: the tropical region at \sim 100 m depth

218 (Fig. 1p); the Alaska Gyre at 200–400 m depth (Fig. 1q–r); the western tropical region at 400–600
219 m depth (Fig. 1r–s); and the Kuroshio–Oyashio transition region at similar depths (Fig. 1r–s). When
220 examined as a function of latitude, the magnitudes of negative O₂ trends do not depend monotonically
221 on latitude alone. While surface-layer declines are strongest at high latitudes, the largest negative
222 trends at intermediate depths (400–600m) occur in the mid-latitude band (30°–40°N). This depth-
223 dependent latitudinal structure implies the importance of remote transports and the circulation-driven
224 redistribution of oxygen, rather than purely local surface forcing. The underlying mechanisms are
225 discussed further in Section 3.3.

226

227 The total uncertainty in dissolved O₂, $u([O_2])_{tot.}$, exhibits pronounced regional structure (Fig. 1v–
228 bb). Uncertainty is largest in the North Pacific north of 50°N and decreases toward lower latitudes.
229 Relatively high uncertainty values are also evident in the surface layer, and within regions of strong
230 density gradients in the eastern tropical Pacific [150°–120°W, 10°–30°N] at depths of 100–200 m (Fig.
231 1w–x). In general, uncertainty peaks near 100 m depth and decreases with increasing depth (Fig. 2
232 and Figure A14 in Sharp et al. [2023]). As shown by Sharp et al. [2023], regionally variations in
233 uncertainty are dominated by algorithmic uncertainty rather than measurement or gridding components
234 (Eq. 1). Elevated algorithmic uncertainty in the northern Pacific above 50°N and along the western
235 and eastern tropical margins below 20°N reflects sparse observational coverage in these regions
236 (Figure 1 in Sharp et al. 2023).

237

238 Compared with the historical horizontal distributions of dissolved O₂ reported by Ito et al. [2017]
239 (Figure 3 in Ito et al. 2017), our analysis reveals a broader spatial extent of negative trends across the
240 North Pacific. Whereas data gaps increase with depth in Ito et al. (2017), the GOBAI-O₂ product
241 provides more spatially continuous coverage, yielding distributions that remain consistent with

242 surrounding regions. In addition, positive O₂ trend detected here in the Kuroshio-Oyashio transition
243 zone and the northeastern North Pacific on density surfaces of 26.8–27.0σ_θ (Fig. 1r) were not clearly
244 evident in the earlier climatology-based analysis. Similarly, the positive trends identified in the western
245 tropical Pacific below 400 m depth (Fig. 1r–t) are stronger and more spatially coherent than those
246 reported previously.

247

248 The positive O₂ trends coincide with regions of relatively low uncertainty values (Fig. 1p–s and 1w–
249 y), suggesting that they are robust features supported by the high observation density of Argo profiling
250 floats. Other regions exhibiting positive signals—the northeastern North Pacific with a density range
251 of 26.8–27.0σ_θ (170°E–150°W, 45–55°N, Fig. 1r) and the tropical western Pacific (130°–170°E, 0°–
252 10°N, Fig. 1r–t)—also correspond to areas of low uncertainty (Fig. 1y–aa). Consequently, these
253 signals likely represent genuine regional reoxygenation superimposed on the basin-scale
254 deoxygenation trend.

255

256 Some localized expansions of the trends, particularly in the tropical eastern Pacific (e.g. 170°–130°W,
257 0°–20°N) may partly reflect regions of elevated uncertainty, occasionally exceeding 15 μmol/kg (Fig.
258 1q–s; Fig. 4i). Such large uncertainties arise from sparse observations and high background variability
259 [Sharp et al. 2023]. Additional bias may stem from sensor calibration limitations in Argo oxygen
260 measurements, especially in oxycline regions where finite optode response times can introduce
261 systematic errors [Bittig et al., 2014; 2018a,b]. Despite these caveats, the spatial patterns of the
262 diagnosed O₂ trends are generally smooth and coherent across the basin. Based on statistical
263 significance testing, most trends are significant throughout the water column (Fig. 1o–u), allowing
264 them to be interpreted in the context of established physical processes in the North Pacific. Overall,

265 the GOBAI-O₂ dataset provides an improved framework for diagnosing basin-scale oxygen variability
266 and its physical drivers.

267

268 **3.2 Vertical sections and isopycnal density analysis of liner trends in 137°E and 165°E lines**

269 To facilitate direct comparison with historical ship-based observations, we examine vertical sections
270 and isopycnal distributions of linear trends in potential temperature, salinity, and dissolved O₂ along
271 the 137°E and 165°E meridional sections (Fig. 3). Ogata and Nonaka [2020] analyzed salinity data
272 from 20 years of shipboard observations along the 137°E line between 1997 and 2016, while Sasano
273 et al. [2015] analyzed temperature, salinity, and dissolved O₂ data from 25 years of cruises along the
274 165°E line between 1987 and 2011.

275

276 Along both sections, large negative trends in potential temperature and salinity are concentrated along
277 the 25.0–26.0σ_θ isopycnal surfaces, corresponding to potential temperatures of approximately 10–
278 12°C and salinities of 34.4–34.5 (Fig. 3a, b, e, f). In contrast, the strongest negative trends in dissolved
279 O₂ occur primarily along denser isopycnals between 26.0 and 27.0σ_θ (Fig. 3c, g). This vertical
280 separation indicates that the regions of pronounced oxygen decline are not co-located with those of
281 temperature and salinity trends, implying distinct controlling mechanisms.

282

283 In addition to widespread oxygen declines, pronounced positive O₂ trends are detected south of ~15°N
284 below 200 m depth along the 137°E line (Fig. 3c). These positive trends are located near the upper
285 boundary of the oxygen minimum layer (OML). Comparison with the corresponding uncertainty
286 distributions (Fig. 3d, h) shows that regions exhibiting positive or negative oxygen trends generally
287 do not coincide with areas of elevated uncertainty, indicating that these signals are robust with the

288 GOBAI-O₂ framework.

289

290 The distributions of linear trends on isopycnal surfaces further highlight differences among
291 temperatures, salinity, and dissolved O₂ (Fig. 4). Trends in temperature and salinity are closely aligned,
292 with warming accompanied by salinification and cooling accompanied by freshening (Fig. 4a–b, d–
293 e). In the tropical region (5°S–5°N), distinct positive trends in both variables are evident over the
294 density range of 22.0–26.0σ_θ. In contrast, little systematic trend is detected in the salinity minimum
295 region (S = 34–34.1) within the density range of 26.5–27.0σ_θ. At higher latitudes (40°–50°N), strong
296 positive trends in both temperature and salinity are observed along the 26.0–27.0σ_θ surfaces (Fig. 4e).

297

298 Dissolved oxygen trends exhibit a markedly different structure. Although negative O₂ trends dominate
299 overall, weak but coherent positive trends appear across the density range 23.0–26.0σ_θ in low-latitude
300 regions (5°S–5°N). More pronounced positive O₂ trends are detected in the deeper density range of
301 26.0–27.0σ_θ between 5° and 10°N. Additional weak positive trends are observed between 10° and
302 20°N within the density range of 23.0–25.0σ_θ along both the 137°E and 165°E sections.

303

304 Compared with previous studies, the GOBAI-O₂-based trends reveal both similarities and notable
305 differences. The general characteristics of temperature and salinity trends are broadly consistent with
306 those reported by Sasano et al. [2015], although the present results are spatially smoother, particularly
307 for dissolved oxygen. This smoothness likely reflects the gridded nature of the dataset and the spatial
308 regularization inherent in the machine-learning reconstruction. Along the 137°E section, the GOBAI-
309 O₂ temperature and salinity fields exhibit a wider area of negative salinity trends within the density
310 range 22.0–24.0 σ_θ than those reported by Ogata and Nonaka [2020] using OFES output.

311

312 Ship-based observations by Sasano et al. [2015] identified patchy positive trends in oxygen within
313 the density range $24.5\text{--}27.5\sigma_\theta$ in the regions ($5^\circ\text{--}15^\circ\text{N}$ and $6^\circ\text{S}\text{--}1^\circ\text{N}$), as well as localized positive
314 trends at greater depths. In contrast, the GOBAI- O_2 data reveal a broader, smoother, and more spatially
315 coherent pattern of positive O_2 trend spanning -6°S to 5°N . At the same time, the present analysis more
316 clearly delineates the core regions of negative oxygen trends between 5° and 15°N along the lower
317 isopycnals (Fig. 3c and f), which are characteristic of the subtropical gyre. These differences
318 underscore the complementary nature of ship-based observations and gridded reconstructions and
319 highlight the advantage of GOBAI- O_2 for resolving basin-scale and isopycnal-scale oxygen variability.

320

321 **3.3 Horizontal distribution of linear trends along isopycnal surfaces**

322 **3.3.1 Potential temperature and salinity**

323 The horizontal distributions of linear trends in potential temperature, salinity, and dissolved oxygen on
324 specific isopycnal surfaces at 25.0 , 26.0 , and $26.8\sigma_\theta$ (Fig. 5) are illustrated to examine how these
325 trends occur and how they are connected. These density surfaces correspond to the shallower density
326 range of Subtropical Mode Water (STMW), the shallower densities of Central Mode Water (CMW)
327 [Suga et al., 1997; 2004], and the representative density of North Pacific Intermediate Water (NPIW)
328 [Nakamura et al., 2000a, b; Nakamura and Awaji, 2003; Yasuda, 2004], respectively. STMW is
329 formed south of the Kuroshio Extension between $30\text{--}35^\circ\text{N}$ and $130\text{--}170^\circ\text{E}$, and reaches depths of
330 approximately 400 m in late winter. It then spreads toward the subtropical front through advection
331 across the Kuroshio recirculation area. CMW is formed in the transition area of the central North
332 Pacific and spreads eastward along the North Pacific Current before turning southward and westward
333 in the subtropical gyre [Suga et al., 1997; 2004]. In contrast, NPIW does not outcrop during its
334 formation process. Its origin lies in Okhotsk Sea Mode Water, which forms through overturning driven
335 by diapycnal upwelling and tidal mixing around the Kuril Islands [Nakamura et al., 2000a, b;

336 Nakamura and Awaji, 2003; You, 2003; Yasuda, 2004] as well as double diffusions in the North Pacific
337 [You, 2003].

338

339 The linear trends on the 25.0, 26.0, and 26.8 σ_θ surfaces show that positive and negative tendencies
340 appear in characteristic locations and are generally aligned with the geostrophic streamlines (Fig. 5a–
341 b, d–e, g–h). Although exceptions exist, such as weak positive trends (150–175°E, 20–30°N) (Fig.
342 5a–b), negative trends in potential temperature and salinity dominate in the western and central North
343 Pacific on the 25.0 and 26.0 σ_θ surfaces (Fig. 5a–b, d–e). Conversely, positive trends in temperature
344 and salinity are most prevalent in the northeastern and/or eastern regions of the basin along the
345 geostrophic streamlines (Fig. 5a–b, d–e). These patterns suggest that waters subducted in the frontal
346 region with reduced temperature and salinity originate mainly from the northeastern North Pacific and
347 are advected southward along the subtropical circulation (Fig. 5a–b, d–e). Exceptions occur in parts
348 of the northeastern basin (170–130°W, 40–60°N), where warmer and more saline waters influence
349 the water masses sinking near the Alaska gyre and subsequently transported outside the subtropical
350 gyre and along the California coast.

351

352 At 26.8 σ_θ (Fig. 5g–h), large positive trends in temperature and salinity are found along the Kuril
353 Islands, with moderate positive trends appearing on the eastern side of the basin, respectively. Waters
354 at this density range (26.8 σ_θ) are not directly ventilated but are formed through diapycnal mixing
355 processes [Nakamura et al., 2000a, b; Nakamura and Awaji, 2003; You, 2003; Yasuda, 2004] and
356 through double diffusion such as salt finger [You, 2003]. Thus, the observed positive temperature and
357 salinity trends at 26.8 σ_θ likely reflect influences from changes occurring in the overlying layers (Fig.
358 5d–e and g–h).

359

360 A meridional northward shift of the outcrop line in the North Pacific associated with recent climate
 361 change has been identified in OFES analyses [Ogata and Nonaka, 2020]. Similar northward shifts of
 362 25.0 and 26.0 σ_θ outcrop lines appear in the present dataset (Fig. 6). These northward displacements
 363 can be attributed to surface warming and increased stratification under global climate change and
 364 provide an explanation for negative temperature and salinity trends observed in the subtropical gyre,
 365 where less saline subarctic-origin waters are subducted and advected southward. The positive
 366 temperature and salinity trends occurring in the Alaska region [160°–130°W, 30°–60°N] (Fig. 5a–b
 367 and d–e) are also consistent with the direct warming effect. The 26.0 σ_θ front exhibits primarily
 368 longitudinal, rather than meridional, shifts between 2004 and 2023 (Fig. 6), suggesting that the
 369 corresponding temperature and salinity changes arise directly from surface warming and freshening,
 370 rather than from density-compensated shifts in water-mass distribution.

371

372 3.3.2 Dissolved oxygen

373 The linear trends in dissolved oxygen on the isopycnal surfaces at 25.0, 26.0, and 26.8 σ_θ exhibit
 374 predominantly negative values across the North Pacific (Fig. 5c, f, and i), although their spatial
 375 distributions are not uniform. Large negative trends are concentrated in the northeastern and eastern
 376 regions and gradually decrease toward the west (Fig. 5q, f, and i). Exceptions occur mainly in the
 377 tropics, where notable positive trends in the western tropical areas on the 26.0 and 26.8 σ_θ surfaces.

378

379 The temporal changes in dissolved oxygen (O_2) were decomposed following the method of Sasano et
 380 al. [2015]. The processes underlying the oxygen tendency equations (Eqs. 2 and 3) are summarized
 381 below. We evaluated each contributing term and examined its relative importance for the dissolved O_2
 382 trends. The total tendency of dissolved oxygen can be expressed as

$$383 \quad \frac{\partial O_2}{\partial t} = \left(\frac{\partial O_2}{\partial z} \frac{\partial z}{\partial t} \right) + \left(\frac{\partial O_2^{sat}}{\partial t} \right)_{net} - \left(\frac{\partial(AOU)}{\partial t} \right)_{net}, \quad (2)$$

384 which can be rearranged as

$$\frac{\partial O_2}{\partial t} = \underbrace{\left(\frac{\partial O_2}{\partial z} \frac{\partial z}{\partial t} \right)}_{(i)} + \underbrace{\left(\frac{\partial O_2^{sat}}{\partial t} - \frac{\partial O_2^{sat}}{\partial z} \frac{\partial z}{\partial t} \right)}_{(iii)} + \underbrace{\left(-\frac{\partial(AOU)}{\partial t} + \frac{\partial(AOU)}{\partial z} \frac{\partial z}{\partial t} \right)}_{(v)}. \quad (3)$$

385
386 (i) (ii) (iii) (iv) (v) (vi)

387 Here, $X = O_2, O_2^{sat}, AOU$ (Apparent Oxygen Utilization). The term $\partial z/\partial t$ denotes the temporal
388 change in the depth of the isopycnal surface (z), while $\partial X/\partial z$ represents the vertical gradient of the
389 variable X at that surface, averaged over the past 20 years. The net tendency term ($\partial X/\partial t$)_{net}
390 represents the net changes associated with a variable X.

391

392 By applying Eq. (3), the rate of O_2 change (term i), which is the rate of reconstructed O_2 data
393 estimated from the linear regression analysis, on each isopycnal surface can be decomposed into
394 contributions from:

395 (term ii) vertical heave acting on the vertical O_2 gradient;

396 (term iii) solubility effects due to temperature and salinity changes;

397 (term iv) vertical heave acting on the solubility gradient;

398 (term v) AOU changes related to air-sea disequilibrium, biological activities, and lateral circulation

399 (term vi) vertical heave acting on AOU gradients.

400 The derivation of Eqs. (2) and (3) follows Sasano et al. [2015] and is described in Appendix. A
401 schematic illustration of this decomposition is provided in Supplementary Figure S5.

402

403 Figure 7 shows the horizontal distributions of the magnitude of each term on $25.0\sigma_\theta, 26.0\sigma_\theta,$ and $26.8\sigma_\theta$
404 surfaces. The results indicate that the prominent O_2 declines (Fig. 5c, f, i) arise from a combination
405 of positive and negative contributions, with the dominant terms varying by latitude. In the high-latitude

406 region around the Alaska Gyre in higher latitudes (170° – 130° W, 40° – 60° N), the largest negative
407 contributions are associated with the deepening of isopycnal surfaces (term ii) and the vertical heave
408 acting on the AOU gradient (term vi) (Fig. 7f, j, k, o). Because the dissolved oxygen generally
409 decreases with depth ($\partial O_2 / \partial z < 0$), deepening of isopycnal surfaces ($\partial z / \partial t > 0$) (Fig. 8 b–c)
410 produces a negative contribution through vertical heave. Similarly, because AOU typically increases
411 with depth, isopycnal deepening leads to an apparent increase in AOU, contributing negatively to
412 dissolved O_2 via term (vi). In contrast, solubility-related changes (term iii) and net AOU tendencies
413 (term v) act in opposite directions during this period (Fig. 7g–h, l–m). Taken together, these results
414 are consistent with the strong negative O_2 trends observed in the Bering Sea on the $26.0\sigma_{\theta}$ and $26.8\sigma_{\theta}$
415 surfaces (150° E– 170° W, 50 – 60° N; Figs. 5f and i).

416

417 In the subtropical and mid-latitudes (10° – 40° N), the O_2 decline is largely associated with AOU
418 changes (term v) (Fig. 7d, i, and n). The relative weakening of the total O_2 decrease in the western
419 North Pacific (Fig. 5c, f, i) coincides with positive contributions from vertical heave of isopycnal
420 surfaces (term ii) (Fig. 7f and k). Additional positive trends arise from solubility-related effects
421 (term iii) (Fig. 7b), and the vertical heave acting on the AOU gradient (term vi) (Fig. 7j and o and
422 Fig. 8b–c).

423

424 In the mid-ocean between 170° E and 160° W, the positive O_2 tendencies transition to weakly negative
425 values. In contrast, a pronounced band of positive trends zonally across the North Pacific Ocean
426 between 30° N and 50° N, primarily associated with the combined effects of terms (iii) and (v) (Fig.
427 7l, h–i, and m–n). This pattern may be related to the northward meridional shift of the subtropical and
428 subarctic frontal zone under recent global warming [Ogata and Nonaka, 2020]. Enhanced winter

429 convection in this region may introduce nutrients into the surface layer, potentially increasing
430 biological activity and AOU. In the NPIW formation region near the Kuril Islands, negative
431 contributions from term (iii) are observed (Fig. 7l), suggesting weaker vertical mixing during the
432 observational period, likely influenced by enhanced surface-layer stratification. This interpretation is
433 supported by the positive trends in temperature and salinity observed in the winter subducted areas
434 [Suga et al., 1997; 2004; Yasuda, 2004] (Fig. 5d–e, g–h).

435

436 In the western tropical Pacific, pronounced increases in dissolved O₂ are observed within the density
437 range of 26.8–27.2 σ_{θ} (Fig. 3c and g; Fig. 4c and g; Fig. 5c, f, and i), overlapping with the OML
438 [Reid, 1997]. Similar features have been reported by Sasano et al. [2015] and Takatani et al. [2012].
439 Variability of the North Equatorial Counter Current (NECC) is likely relevant in this region.
440 According to the study of Chen et al. [2016] based on the OFES outputs including a multidecadal
441 variability (1960–2014), the NECC exhibits two distinct modes of variability: an interannual mode
442 characterized by strengthening accompanied by southward migration, and an interdecadal mode
443 marked by a gradual weakening, poleward migration, and broadening.

444

445 The validity of time-varying signals in the western tropical Pacific in the OFES data has been
446 demonstrated by Chen et al. [2016]. We further examined the longer-term OFES data (1950–2023),
447 as well, for poleward, eastward velocities, as well as potential temperature and salinity here (Fig. 9c,
448 g). Positive temperature anomalies in 0°–5 °N occur above 250 m depth, while negative anomalies
449 appear along the 26.0 σ_{θ} surface between 5°–20°N, a similar pattern that is also evident in the GOBAI-
450 O₂ data (Fig. 3a). A discrepancy is found in salinity trends: GOBAI-O₂ shows negative trends along

451 $26.0\sigma_\theta$ (Fig. 3b), whereas OFES exhibits positive trends (Fig. 9b, f), likely reflecting higher salinity
452 at 200–600 m depth in OFES between 0° and 7°N (Fig. 10b, d).

453

454 Anomalies in poleward and eastward velocities (Fig. 9a–b, e–f and Fig. 11a–b) indicate enhanced
455 poleward flow around 5°N above 200m depth and a poleward shift of the eastward velocity core. These
456 changes are consistent with the interdecadal mode of NECC variability described by Chen et al.
457 [2016]. The broadening of the NECC was less evident here, possibly because the present analysis
458 uses raw velocity fields rather than isolating the second EOF modes. The wind-stress curl over the
459 equatorial Pacific shows a persistent decrease and poleward expansion of negative values along the
460 0° – 10°N from 1950 to 2023 (Fig. 12).

461

462 The westward penetration of the OML is slow and occurs between two eastward-extending tongues of
463 high O_2 water originating near the equator [Reid, 1997] (Fig. S6). The observed O_2 increase on the
464 26.8 – $27.2 \sigma_\theta$ surfaces (Fig. 3c, g and Fig. 4c, g) is consistent with a weakening and north-poleward
465 shift of the interdecadal NECC mode. The subsurface O_2 increase, particularly below 400m depth (Fig.
466 1r–u), is therefore likely influenced by these circulation changes, potentially allowing higher- O_2 water
467 to extend westward (Fig. S6). In addition, shoaling of isopycnal surfaces near the equator indicates a
468 northward shift of the boundary between the tropical and subtropical gyres along 137°E line during
469 the observational period.

470

471 **4. Discussion and Conclusion**

472 The variability of dissolved oxygen in the North Pacific reflects the combined influences of global

473 warming and climate variability. In this study, we used the four-dimensional GOBAI-O₂ dataset -
474 constructed using machine -learning methods applied to historical temperature, salinity, and oxygen
475 observations from BGC-Argo floats and ship-based measurements—to examine linear trends in
476 potential temperature, salinity, and dissolved oxygen over the past two decades (2004–2023). The
477 linear trends are broadly consistent with findings from previous studies [Takatani et al. 2012; Sasano
478 et al. 2015; Ogata and Nonaka, 2020], and we clarified how these trends vary spatially (Figs. 3 and
479 4).

480

481 An important outcome of this study is that GOBAI-O₂, being globally gridded, allows spatially
482 continuous and smooth representations of trends, both horizontally and vertically, across the North
483 Pacific. This provides a more coherent picture than earlier datasets that relied solely on sparse ship-
484 based observations. The horizontal trend patterns mapped on isopycnal surfaces (Fig. 5) show that
485 dissolved oxygen exhibits a basin-scale decreasing trend. At the same time, several regions display
486 locally increasing oxygen, including areas influenced by the meridional migration of subtropical and
487 subpolar fronts (Fig. 4). The strong positive oxygen trends in the western equatorial region are
488 consistent with a weakening of the second mode of the NECC variability. The decomposition analysis
489 further illustrates how each physical component contributes to oxygen changes along isopycnal
490 surfaces (Fig. 7).

491

492 Although many of the large-scale features identified here resemble those reported by Ito et al. [2017],
493 our analysis reveals regional and isopycnal-scale structures that were previously unresolved. In
494 particular, the positive oxygen trends in the Kuroshio–Oyashio Transition Zone, the northeastern North
495 Pacific along the 26.8–27.0 σ_θ density surfaces, and the enhanced subsurface O₂ increase in the tropical
496 western Pacific below 400 m were not clearly distinguished in earlier climatology-based studies. These

497 improvements arise because GOBAI-O₂ integrates high-frequency BGC-Argo oxygen observations
498 with a spatially consistent mapping scheme, reducing observational gaps and sampling biases in
499 dynamically active regions. This demonstrates that regional reoxygenation signals can coexist with
500 large-scale deoxygenation, and highlights the importance of sustained BGC-Argo observations for
501 detecting emerging changes in ocean biogeochemistry.

502

503 Recent work by Bushinsky et al. [2025] has reported the presence of a systematic negative bias
504 (approximately -2.7 $\mu\text{mol kg}^{-1}$) in air-calibrated BGC-Argo oxygen measurements compared with
505 ship-based reference profiles. This bias does not appear to be explicitly corrected in the GOBAI-O₂,
506 and therefore may affect the magnitude of the estimated oxygen trends—potentially enhancing negative
507 trends or suppressing positive ones in regions with dense float sampling. Such biases may also
508 influence the apparent vertical structure of oxycline. In the North Pacific, regions with high float
509 density—such as the Kuroshio–Oyashio transition zone, the North American coastal region, and the
510 vicinity of Hawaii—may be particularly affected (see Fig. 1 of Sharp et al., 2023). While a constant
511 offset would not directly alter linear trend estimates, any time-varying bias associated with sensor
512 behavior or sampling depth could introduce spurious trends. A quantitative evaluation is not feasible
513 at present due to the lack of temporally continuous ship-based reference data at the spatial scales. This
514 limitation should therefore be kept in mind when interpreting the O₂ trends reported here.

515

516 It is also essential to recognize that GOBAI-O₂ is a machine learning reconstruction derived from
517 available temperature, salinity, and oxygen measurements. While this approach significantly enhances
518 special coverage, the results should be interpreted cautiously. Importantly, however, such
519 methodological uncertainties are unlikely to alter the large-scale spatial coherence of the trend patterns
520 identified in this study. Nevertheless, future work incorporating improved calibration of Argo oxygen
521 sensors, expanded ship-based reference datasets, independent machine learning reconstructions [e.g.,

522 Ito et al., 2024], and comprehensive ocean reanalysis will be necessary to better constrain these
523 uncertainties.

524

525 The monthly mean climatological GOBAI-O₂ data set should include the Pacific Decadal Oscillation
526 (PDO; Stramma et al., 2020; Pozo Buil and Di Lorenzo, 2017) and the North Pacific Gyre Oscillation
527 (NPGO; Stramma et al., 2020). This dataset, therefore, provides a valuable basis for examining how
528 such climate variation influences dissolved oxygen through physical driving mechanisms.
529 Investigating these relationships more explicitly will be an important direction for future research.

530

531

532 **Data availability**

533 GOBAI-O₂ data is available at [https://www.ncei.noaa.gov/access/metadata/landing-](https://www.ncei.noaa.gov/access/metadata/landing-page/bin/iso?id=gov.noaa.nodc:0259304)
534 [page/bin/iso?id=gov.noaa.nodc:0259304](https://www.ncei.noaa.gov/access/metadata/landing-page/bin/iso?id=gov.noaa.nodc:0259304). Temperature and salinity are from Roemmich and Gilson
535 [2009] Argo climatology (https://sio-argo.ucsd.edu/RG_Climatology.html). The OFES and NCEP-
536 NCAR data used in our study are obtained from APDRC, University of Hawaii ([http://apdrc-](http://apdrc.soest.hawaii.edu)
537 [soest.hawaii.edu](http://apdrc.soest.hawaii.edu)).

538

539 **Author contributions**

540 MI designed the study, performed the analyses, and prepared all figures. MI wrote the initial draft of
541 the manuscript. MI and TO contributed to the interpretation of the results. All authors contributed to
542 improving the manuscript.

543

544 **Acknowledgements:**

545 Jonathan D. Sharp and the reviewers are acknowledged for providing comments that prompted

546 significant improvements to this manuscript.

547

548

549 **Financial support:**

550 This research has been supported by the Institute for Basic Science (grant no. IBS-R028-D1) and the

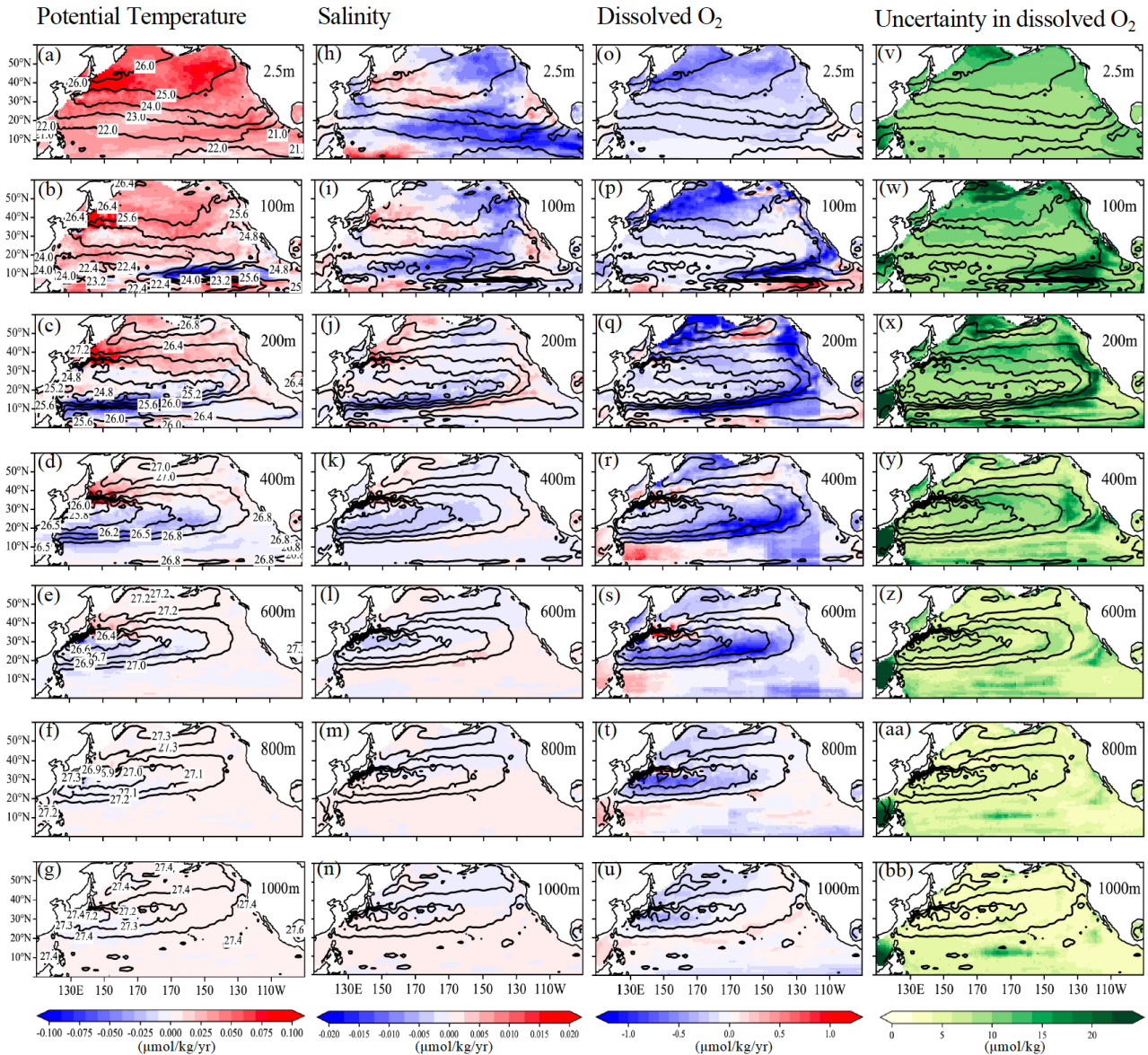
551 Japan Society for the Promotion of Science (JSPS) through a Grant-in-Aid for Scientific Research

552 JP22H00176.

553

554 **Figure captions:**

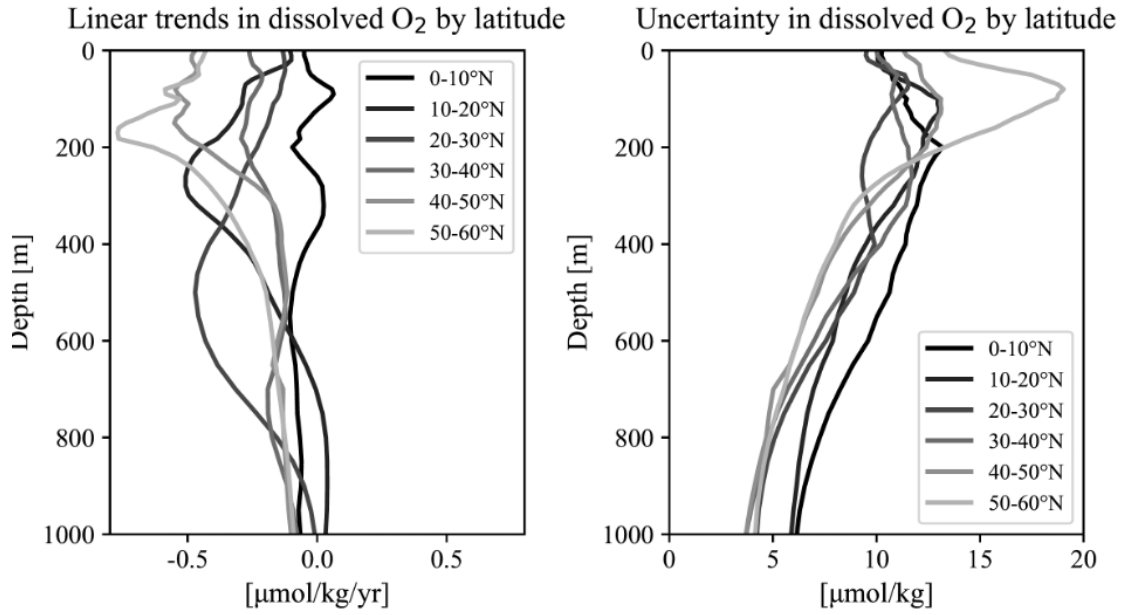
555



556

557 **Figure 1** Horizontal distributions of linear trends ($\mu\text{mol/kg/yr}$) in (a–g) potential temperature, (h–n)
 558 salinity, and (o–u) dissolved oxygen (O_2) during the observational period at depths of 0, 100, 200,
 559 400, 600, 800, and 1000 m, respectively. Contours denote potential density at each depth. Labels for
 560 the potential density are shown only in the potential temperature sections. Corresponding distributions
 561 of the mean uncertainty in dissolved O_2 ($\mu\text{mol/kg}$) are presented in panels (v–bb).

562



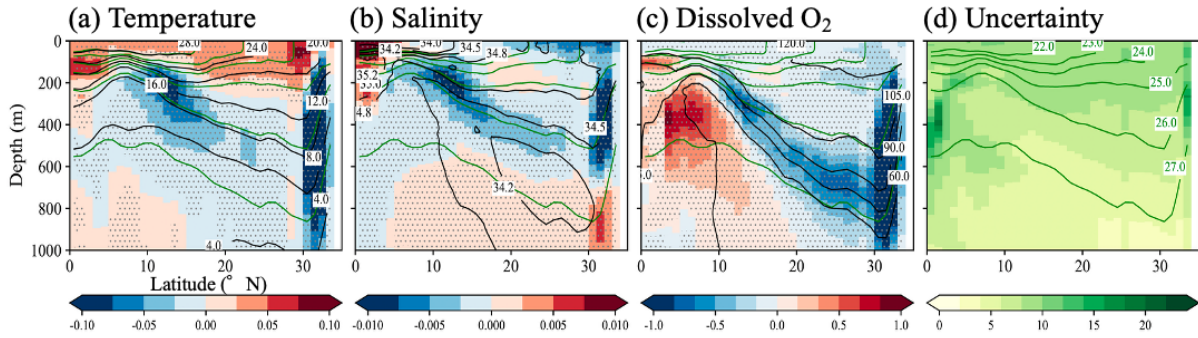
563

564 **Figure 2** Vertical profiles of linear trends and uncertainty in dissolved O₂ by latitude.

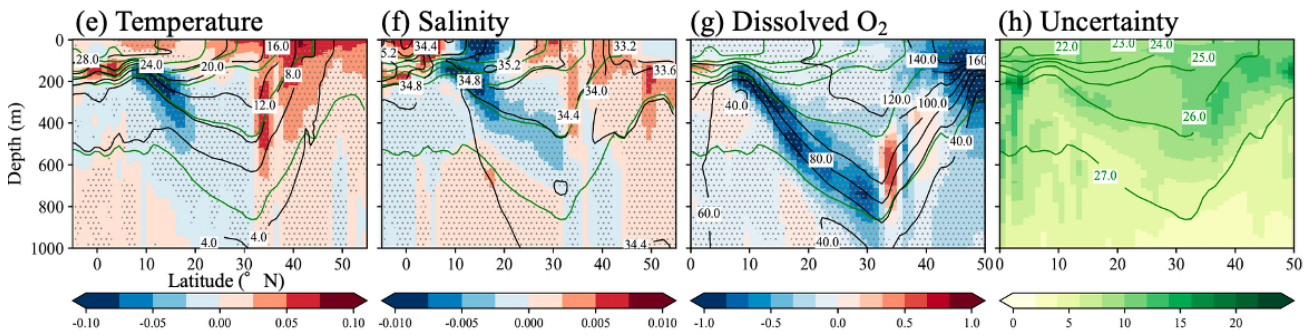
565

566

137° E line



165° E line



567

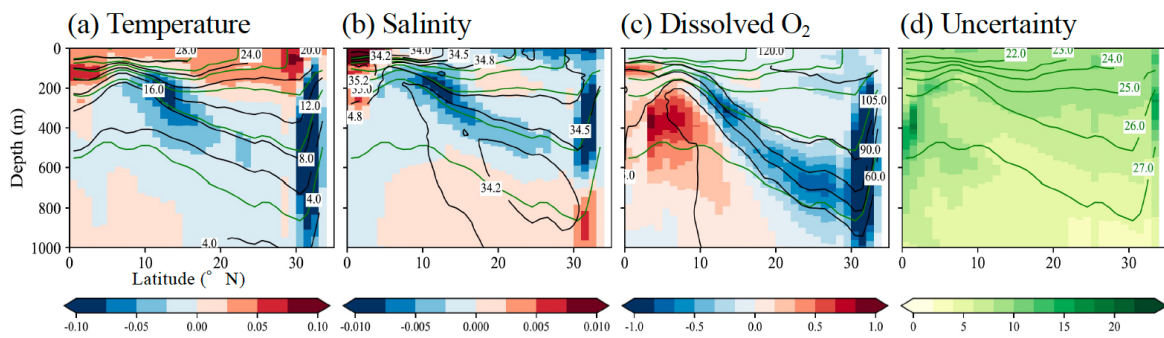
568 **Figure 3** Vertical sections showing linear trends in potential temperature (a, e), salinity (b, f), and

569 dissolved O₂ (c, g) along the 137°E and 165°E meridians, respectively. Corresponding vertical
 570 sections of the mean uncertainty are presented in panels (d) and (h). Black contour lines indicate the
 571 mean potential temperature (a, e), salinity (b, f), and dissolved oxygen (c, g) over the period 2004–
 572 2023, while green contour lines represent the mean potential density. Labels for the potential density
 573 are shown only in the uncertainty sections.

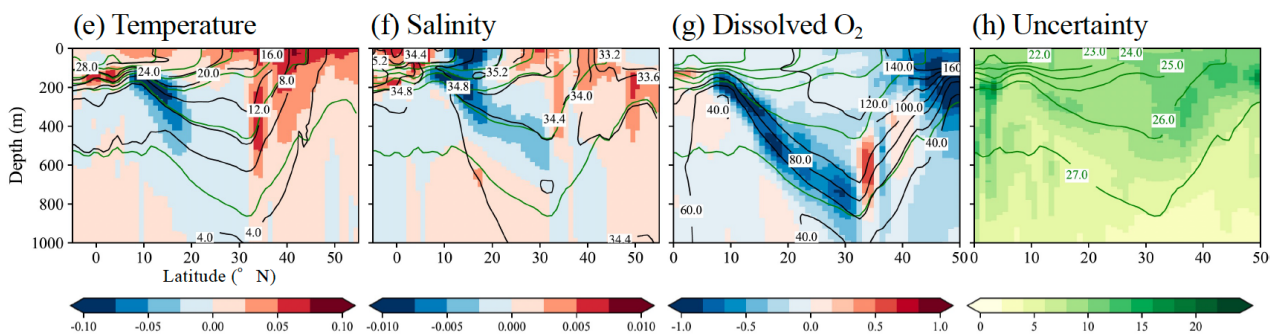
574

575

137° E line



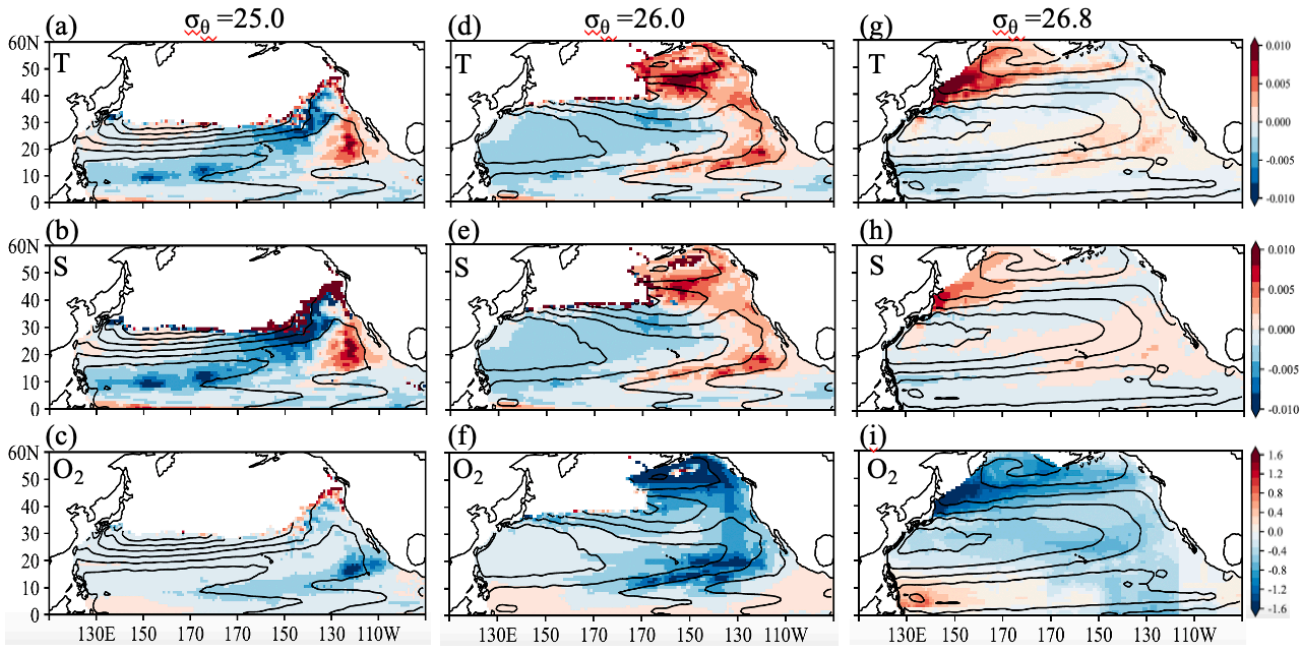
165° E line



576

577 **Figure 4** Linear trends in (a, e) potential temperature, (b, f) salinity, (c, g), and dissolved O₂ on each
 578 isopycnal surface at intervals of $0.1\sigma_\theta$, calculated at every 1.0 deg of latitude in 137 °E and 165 °E
 579 lines, respectively. Contour lines represent the mean values during the target observation periods,
 580 plotted at intervals of $0.1\sigma_\theta$ for each 1 deg. of latitude. Fig. 4 (d) and 4 (h) are the same but show
 581 the averaged uncertainty during the target observation periods, on each isopycnal surface.

582

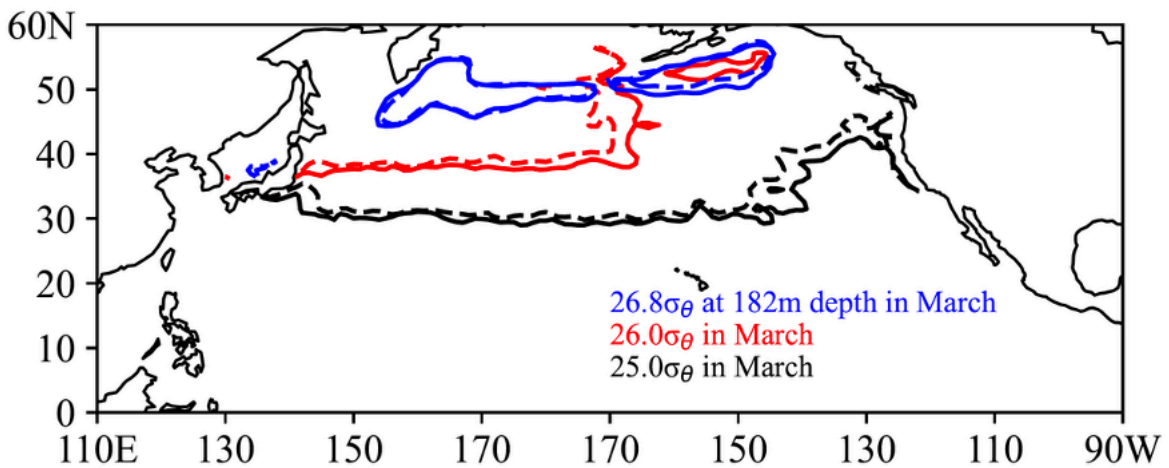


583

584 **Figure 5** Linear trends in (a) potential temperature, (b) salinity, and (c) dissolved O₂ on each
 585 isopycnal surface at 25.0, 26.0, and 26.8σ_θ. Contour lines represent geostrophic flow streamlines on
 586 26.0 and 26.8σ_θ surfaces, relative to 2000 m.

587

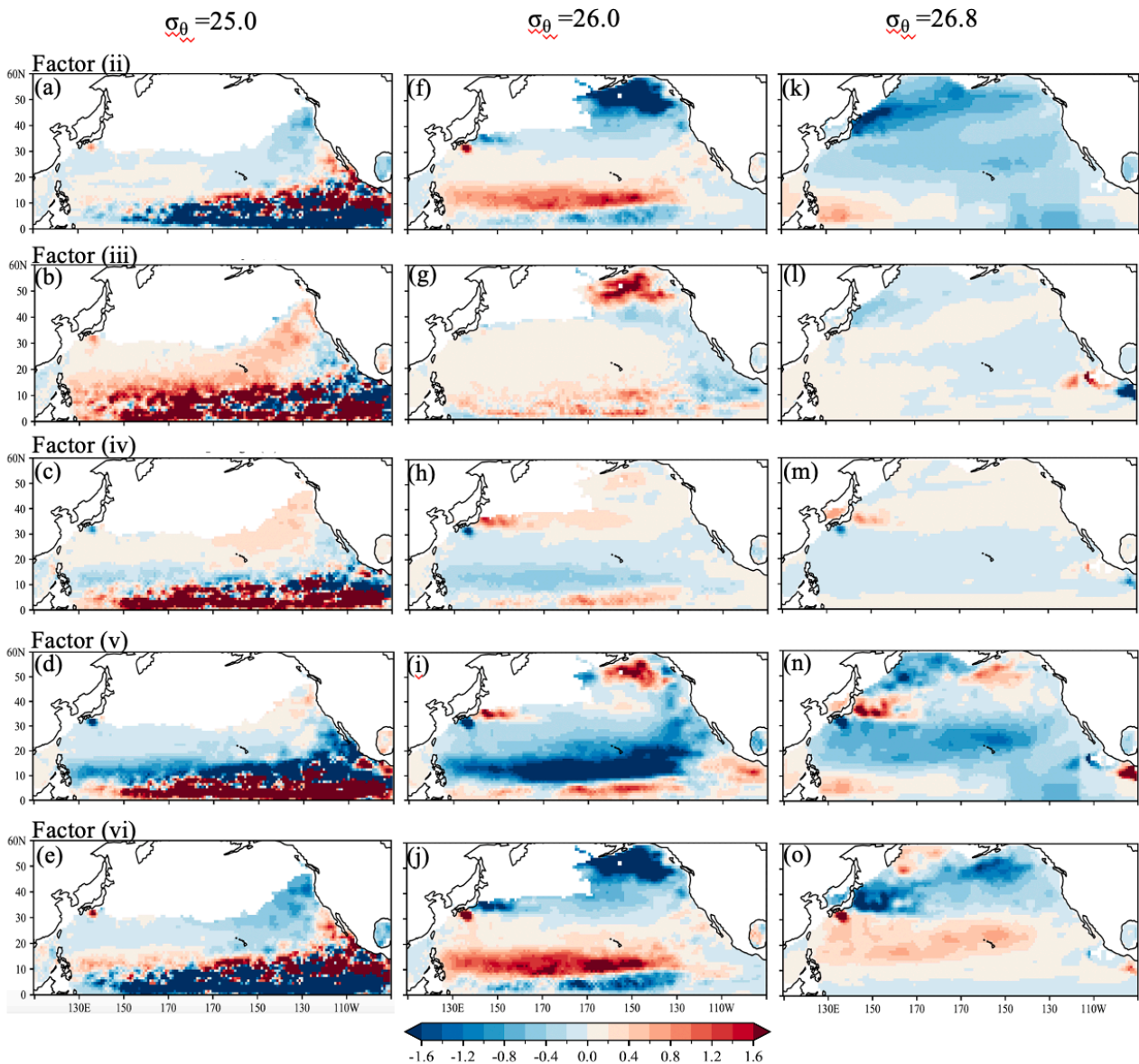
588



589

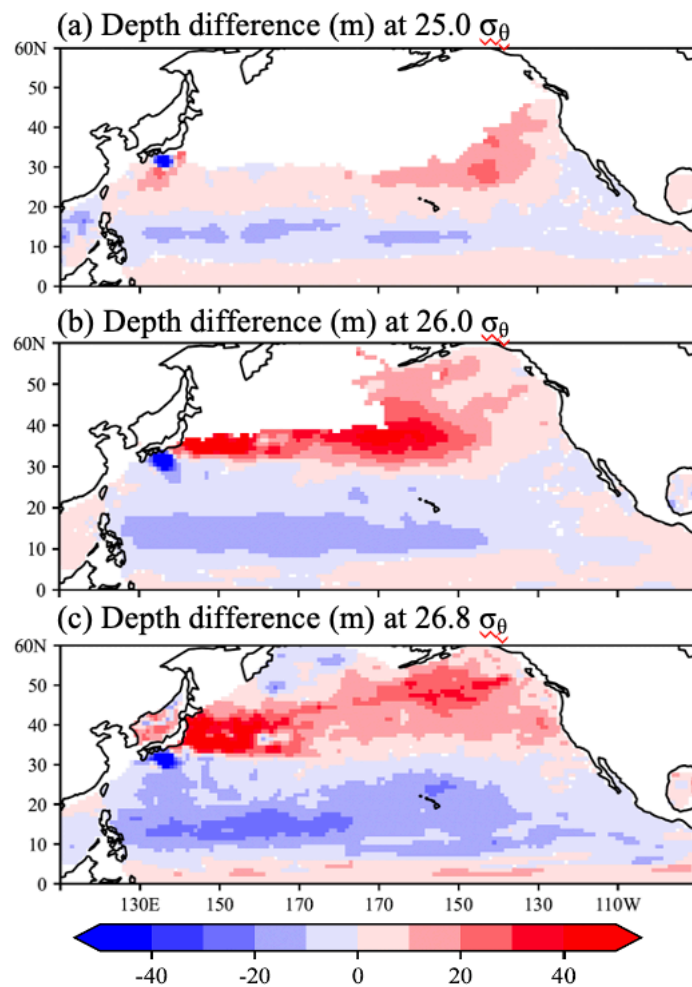
590 **Figure 6** Density contours of 25.0σ_θ (black), 26.0σ_θ (red), and 26.8σ_θ (blue). Solid lines indicate
 591 the average density contours for March 2004–2009, while dashed lines represent 2019–2023.

592



593

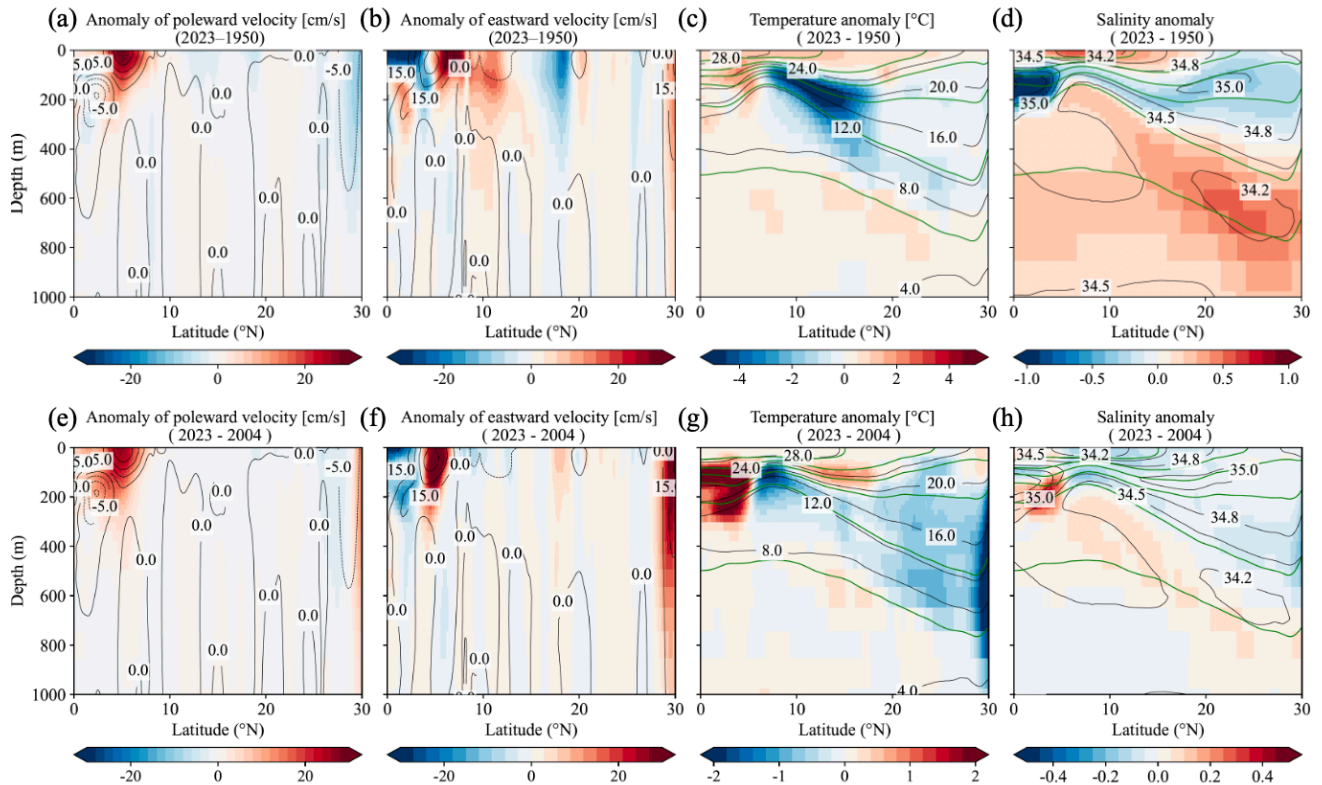
594 **Figure 7** Horizontal distributions of the magnitude of each factor contributing to the rate of O_2 change
 595 on 25.0, 26.0, and 26.8 σ_θ in Eq. (1). The rate of O_2 change on each isopycnal surface is decomposed
 596 into the following components: (ii) the apparent contribution from vertical heave (deepening or
 597 shoaling) of isopycnal surfaces associated with warming and/or surface freshening; (iii) the
 598 contribution from changes in oxygen solubility (O_2^{sat}) associated with temperature and salinity
 599 variations; (iv) the contribution from vertical heave acting on the background solubility gradient;
 600 (v) the contribution from net changes in apparent oxygen utilization (AOU) associated with air–sea
 601 disequilibrium, biological activity, and lateral advection and/or circulation; and (vi) the contribution
 602 from vertical heave acting on AOU gradients, independent of solubility changes. This decomposition
 603 is applied to the reconstructed dissolved oxygen fields obtained from linear regression analysis.



605

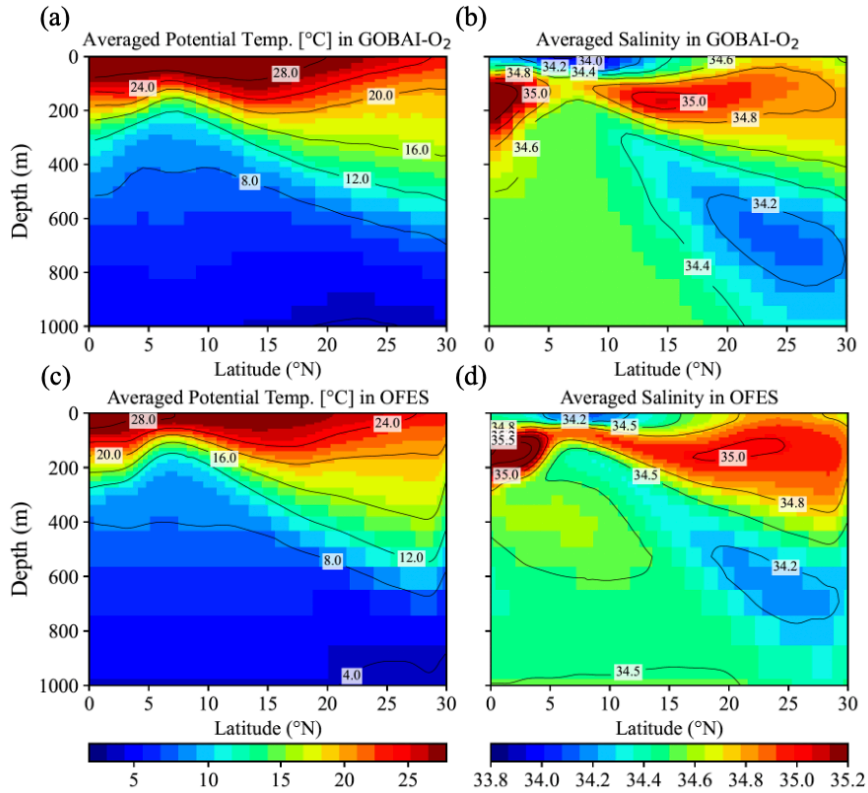
606 **Figure 8** Depth difference (m) between the 5-year averaged data in March, 2004–2009 and 2018–
 607 2023 at 25.0 , 26.0 , and $26.8\sigma_{\theta}$. The reconstructed O_2 data estimated from the linear regression analysis
 608 were used in this calculation. Positive and negative values indicate the deepening and shallowing,
 609 respectively, from the depth of each density in 2004– 2023.

610



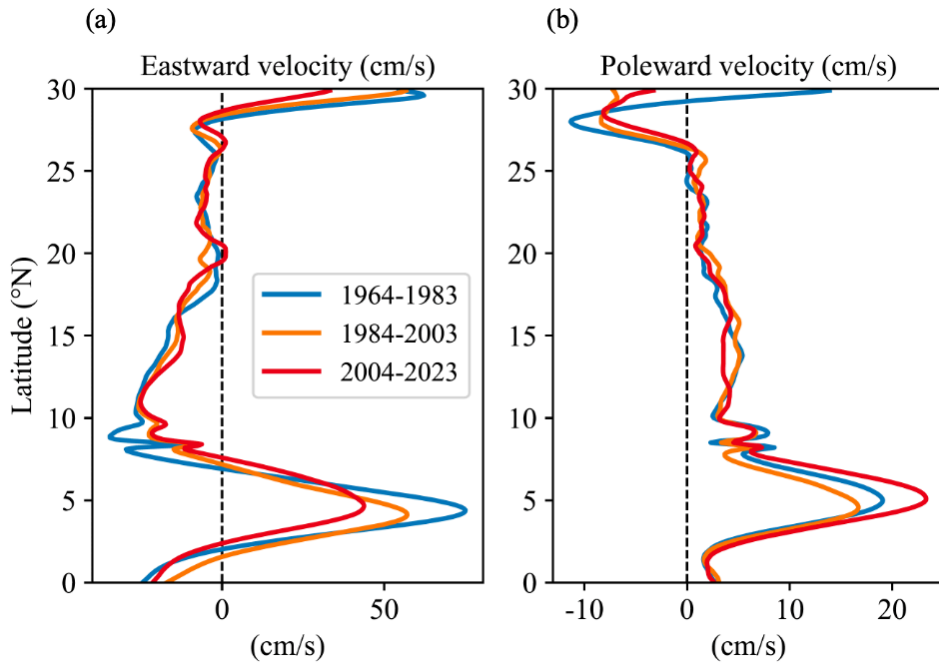
611

612 **Figure 9.** Anomaly of poleward and eastward velocity, potential temperature, and salinity in the OFES
 613 model outputs from 1950 to 2023 (a–d) and from 2004 to 2023 (e–h), respectively, in the 137°E line.
 614 Contours of averaged values of poleward and eastward velocity, potential temperature, and salinity
 615 during the target period are also shown in each figure. Green contour lines in (c–d, g–h) indicate the
 616 average potential density of 22, 23, 24, 25, 26, and 27 σ_{θ} , during the target periods.



617

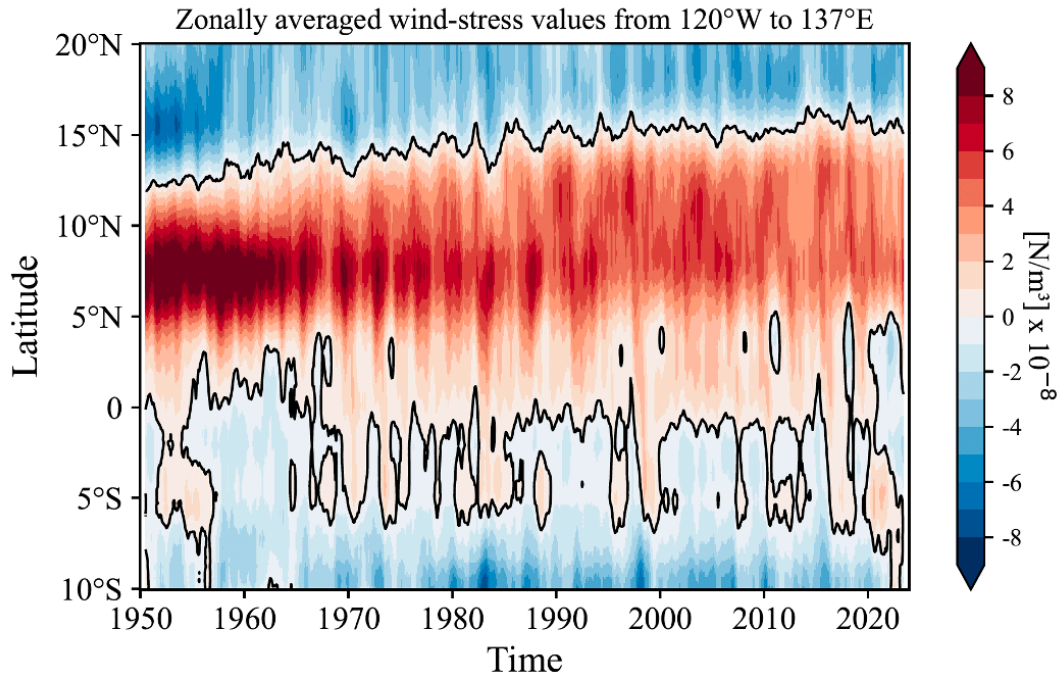
618 **Figure 10.** Averaged Potential Temperature (a, c) and salinity (b, d) in GOBAI-O₂ from 2004 to
 619 2023 and OFES data from 1950 to 2023, respectively, in the 137°E line.



620

621 **Figure 11.** Latitudinal distribution of averaged eastward (a) and poleward velocity (b) in the OFES
 622 data from 1964 to 1983, from 1984 to 2003, and from 2004 to 2023, respectively, in the 137°E line.

623



624

625 **Figure 12.** NCEP-NCAR wind-stress curl values zonally averaged from 137°E to 120° W from 1950
 626 to 2023. A 13-month running-mean filter has been applied in time.

627

628 **Appendix: Essential concepts and derivations for Equation (2–3)**

629 The essential concepts and derivations for equations (2) and (3) were originally proposed by Takatani
 630 et al. [2012] and subsequently described in detail by Sasano et al. [2015]. Here, we briefly summarize
 631 and follow their derivation.

632

633 When the temperature at a depth z_A increases from θ_A to θ_A' as a result of increased ocean heat
 634 content, the density at that depth decreases from σ_A to σ_A' . For simplicity, the vertical salinity profile
 635 is assumed to remain unchanged with time. As a consequence, the isopycnal surface of σ_A deepens
 636 from z_A to z_B (Figure S5). If surface freshening occurs simultaneously due to a net freshwater input,
 637 both the density decreases at z_A (from σ_A to σ_A') and the deepening of the isopycnal surface (from
 638 z_A to z_B) are enhanced. Because density is a function of temperature and salinity ($\sigma = f(\theta, S)$), the

639 density of the isopycnal surface σ_A can be expressed as

640
$$\sigma_A = f(\theta_A, S_A) \quad (\text{before warming}) \quad (\text{C1})$$

641
$$= f(\theta_B', S_B). \quad (\text{after warming}) \quad (\text{C2})$$

642 Here, S_A and S_B denote salinity at depth z_A and z_B , respectively, and θ_B' represents the temperature at
643 density σ_A at depth z_B after warming. The depth z_B is determined by satisfying Eqs. (C1) and (C2).
644 In the region where salinity decreases with depth (e.g., above the salinity minimum layer of NPIW),
645 $S_A > S_B$, and therefore $\theta_A > \theta_B'$. This implies that the potential temperature on an isopycnal surface
646 effectively decreases as a consequence of warming, and that biogeochemical properties on the same
647 isopycnal surface are also expected to change.

648

649 For a tracer X whose vertical profile with respect to depth does not change with time (e.g., salinity;
650 see Figure S5 (c)), the temporal change of X on the potential density surface σ_A is attributed solely
651 to the apparent change caused by the deepening of the isopycnal surface from z_A to z_B :

652
$$\frac{\partial X}{\partial t} = \left(\frac{\partial X}{\partial z} \cdot \frac{\partial z}{\partial t} \right) \quad (\text{C3})$$

653 Here, $\partial X/\partial t$ represents the temporal change of X observed on σ_A (gray arrows in Figure S5), z
654 denotes the depth of σ_A , $\partial X/\partial z$ is the vertical gradient of X with respect to the depth (assumed to be
655 time-invariant), and $\partial z/\partial t$ is the rate of deepening of the isopycnal surface σ_A . The product
656 $\partial X/\partial z \cdot \partial z/\partial t$ represents the effect of isopycnal deepening (white arrows in Figure S5),
657 corresponding to the difference between the filled square and filled circle.

658

659 For a variable Y whose vertical profile evolves with time while warming occurs simultaneously, the
660 temporal change of Y on the density surface σ_A can be expressed as the sum of two components: the
661 contribution due to the isopycnal deepening from z_A to z_B and the net temporal change of Y ,

662 $(\partial Y/\partial t)_{net}$ between the time before and after warming:

663
$$\frac{\partial Y}{\partial t} = \left(\frac{\partial Y}{\partial z} \cdot \frac{\partial z}{\partial t} \right) + \left(\frac{\partial Y}{\partial t} \right)_{net} \quad (C4)$$

664 To evaluate the net change $(\partial Y/\partial z)_{net}$ (illustrated by the blue arrows of a difference in symbols
665 between filled square and open square in Figure S5), it is necessary to evaluate the contribution of the
666 temporal change of Y due to the isopycnal deepening and to subtract it from the change of Y observed
667 at density σ_A . For instance, the change of O_2^{sat} in Figure S5 (f) is observed along the gray isopycnal
668 surface (large white arrow), whereas the net change (large blue and pink arrows) is obtained as the
669 difference between the observed change and the deepening effect.

670

671 The dissolved oxygen concentration O_2 can be expressed as:

672
$$O_2 = O_2^{sat} - AOU, \quad (C5)$$

673 where O_2^{sat} is the oxygen saturation concentration (a function of temperature and salinity), and AOU
674 is “apparent oxygen utilization”, representing the oxygen consumed by biological processes since
675 subduction. Near the surface, AOU is typically small, and its contributions can be neglected.

676

677 Following Eq. (C4), the temporal change of O_2 on a given isopycnal surface at a fixed station is:

678
$$\frac{\partial O_2}{\partial t} = \left(\frac{\partial O_2}{\partial z} \cdot \frac{\partial z}{\partial t} \right) + \left(\frac{\partial O_2}{\partial t} \right)_{net}. \quad (C6)$$

679 Similarly,

680
$$\frac{\partial O_2^{sat}}{\partial t} = \left(\frac{\partial O_2^{sat}}{\partial z} \cdot \frac{\partial z}{\partial t} \right) + \left(\frac{\partial O_2^{sat}}{\partial t} \right)_{net}, \quad (C7)$$

681 and

682
$$\frac{\partial AOU}{\partial t} = \left(\frac{\partial(AOU)}{\partial z} \cdot \frac{\partial z}{\partial t} \right) + \left(\frac{\partial(AOU)}{\partial t} \right)_{net}. \quad (C8)$$

683 The term $(\partial O_2^{sat}/\partial t)_{net}$ is directly related to warming, because O_2^{sat} depends on temperature and
 684 salinity. If AOU does not change with time, that is, if changes in O_2 arise solely from changes in O_2^{sat} ,
 685 then $\partial(AOU)/\partial t$ follows Eq. (C3) and $(\partial(AOU)/\partial t)_{net} = 0$. If AOU varies with time, however,
 686 $\partial(AOU)/\partial t$ follows Eq. (C4) and $(\partial(AOU)/\partial t)_{net} \neq 0$, as illustrated by the dashed gray line in
 687 Figure S5 (g).

688

689 Because O_2 is defined by Eq. (C5), the net temporal change of O_2 on an isopycnal surface is

$$690 \quad \left(\frac{\partial O_2}{\partial t}\right)_{net} = \left(\frac{\partial O_2^{sat}}{\partial t}\right)_{net} - \left(\frac{\partial(AOU)}{\partial t}\right)_{net}. \quad (C9)$$

691 Combining Eqs. (C6) and (C9), the total temporal change of O_2 on an isopycnal surface can be
 692 written as

$$693 \quad \left(\frac{\partial O_2}{\partial t}\right) = \left(\frac{\partial O_2}{\partial z} \cdot \frac{\partial z}{\partial t}\right) + \left(\frac{\partial O_2^{sat}}{\partial t}\right)_{net} - \left(\frac{\partial(AOU)}{\partial t}\right)_{net}, \quad (C10)$$

694 which corresponds to Eq. (1) in the main text. Eq. (C10) corresponds to an arrow in Figure S5 (e),
 695 represented from left to right by the large gray arrow, white, blue, and pink arrows. The large blue
 696 arrow is identical to Figure S5 (f), while the large pink arrow corresponds to Figure S5(g), but with
 697 its direction reversed. Finally, substituting Eqs. (C7) and (C8) into (C10)

$$698 \quad \frac{\partial O_2}{\partial t} = \underbrace{\left(\frac{\partial O_2}{\partial z} \frac{\partial z}{\partial t}\right)}_{(i)} + \underbrace{\left(\frac{\partial O_2^{sat}}{\partial t} - \frac{\partial O_2^{sat}}{\partial z} \frac{\partial z}{\partial t}\right)}_{(iii)} - \underbrace{\left(\frac{\partial(AOU)}{\partial t} - \frac{\partial(AOU)}{\partial z} \frac{\partial z}{\partial t}\right)}_{(v)}, \quad (C11)$$

$$699 \quad \quad \quad (ii) \quad \quad \quad (iv) \quad \quad \quad (vi)$$

700 which corresponds to Eq. (2) in the main text. Note: The signs in terms (v) and (vi) in Eq. (3) are
 701 reversed relative to those in Eq. (C11) for convenience.

702

703 Table A1 The physical interpretation of each term in the oxygen tendency decomposition shown in Eq. (3) and
 704 Eq. (C11) is summarized.

Term	Mathematical form	Physical interpretation
(ii)	$(\partial O_2 / \partial z)(\partial z / \partial t)$	Vertical heave acting on the O ₂ gradient
(iii)	$\partial O_2^{sat} / \partial t$	Solubility effect due to temperature and salinity changes
(iv)	$-(\partial O_2^{sat} / \partial z)(\partial z / \partial t)$	Vertical heave acting on the solubility gradient
(v)	$\partial AOU / \partial t$	AOU changes related to air–sea disequilibrium, biological activity and lateral circulation
(vi)	$-(\partial AOU / \partial z)(\partial z / \partial t)$	Vertical heave of the AOU gradient

705

706 **Data availability:**

707 GOBAI-O₂ [Sharp et al. 2022; 2023] can be accessed from NOAA's National Centers for
 708 Environmental Information at <https://accession.nodc.noaa.gov/0259304> (doi: 10.25921/z72m-yz67).

709

710 **References:**

711 Alkire, M. B., D'Asaro, E., Lee, C., Jane Perry, M., Gray, A., Cetinić, I., et al. (2012). Estimates of
 712 net community production and export using high-resolution, Lagrangian measurements of O₂, NO₃⁻,
 713 and POC through the evolution of a spring diatom bloom in the North Atlantic. *Deep Sea Research*
 714 *Part I: Oceanographic Research Papers*, 64, 157–174. <https://doi.org/10.1016/j.dsr.2012.01.012>

715 Berman-Frank, I., Lundgren, P., & Falkowski, P. (2003). Nitrogen fixation and photosynthetic oxygen
 716 evolution in cyanobacteria. *Research in Microbiology*, 154(3), 157–164.
 717 [https://doi.org/10.1016/S0923-2508\(03\)00029-9](https://doi.org/10.1016/S0923-2508(03)00029-9)

718 Bittig, H. C., Fiedler, B., Scholz, R., Krahnemann, G., & Körtzinger, A. (2014). Time response of oxygen
 719 optodes on profiling platforms and its dependence on flow speed and temperature. *Limnology and*
 720 *Oceanography: Methods*, 12(8), 617–636. <https://doi.org/10.4319/lom.2014.12.617>

721 Bittig, H. C., & Körtzinger, A. (2015). Tackling Oxygen Optode Drift: Near-Surface and In-Air
722 Oxygen Optode Measurements on a Float Provide an Accurate in Situ Reference.
723 <https://doi.org/10.1175/JTECH-D-14-00162.1>

724 Bittig, H. C., Körtzinger, A., Neill, C., van Ooijen, E., Plant, J. N., Hahn, J., et al. (2018a). Oxygen
725 Optode Sensors: Principle, Characterization, Calibration, and Application in the Ocean. *Frontiers in*
726 *Marine Science*, 4. <https://doi.org/10.3389/fmars.2017.00429>

727 Bittig, H. C., Steinhoff, T., Claustre, H., Fiedler, B., Williams, N. L., Sauzède, R., et al. (2018b). An
728 Alternative to Static Climatologies: Robust Estimation of Open Ocean CO₂ Variables and Nutrient
729 Concentrations From T, S, and O₂ Data Using Bayesian Neural Networks. *Frontiers in Marine*
730 *Science*, 5. <https://doi.org/10.3389/fmars.2018.00328>

731 Bopp, L., Resplandy, L., Orr, J. C., Doney, S. C., Dunne, J. P., Gehlen, M., et al. (2013). Multiple
732 stressors of ocean ecosystems in the 21st century: projections with CMIP5 models. *Biogeosciences*,
733 10(10), 6225–6245. <https://doi.org/10.5194/bg-10-6225-2013>

734 Boyer, T. P., and S. Levitus (1997), Objective Analyses of Temperature and Salinity for the World
735 Ocean on a 1/48 Grid, vol. 11, NOAA Atlas NESDIS, Natl. Oceanic and Atmos. Admin., Silver Spring,
736 Md.

737 Boyer, T. P., Antonov, J. I., Baranova, O. K., Coleman, C., Garcia, H. E., Grodsky, A., et al. (2013).
738 World Ocean Database 2013. Retrieved from
739 <https://repository.oceanbestpractices.org/handle/11329/357>

740 Breiman, L. (2001). Random Forests. *Machine Learning*, 45(1), 5–32.
741 <https://doi.org/10.1023/A:1010933404324>

742 Breitburg, D., Levin, L. A., Oschlies, A., Grégoire, M., Chavez, F. P., Conley, D. J., et al. (2018).
743 Declining oxygen in the global ocean and coastal waters. *Science*, 359(6371), eaam7240.
744 <https://doi.org/10.1126/science.aam7240>

745 Bushinsky, S. M., Emerson, S. R., Riser, S. C., & Swift, D. D. (2016). Accurate oxygen measurements
746 on modified Argo floats using in situ air calibrations. *Limnology and Oceanography: Methods*, 14(8),
747 491–505. <https://doi.org/10.1002/lom3.10107>

748 Bushinsky, S.M., Nachod, Z., Fassbender, A.J., Tamsitt, V., Takeshita, Y., Williams, N., 2025. Offset
749 Between Profiling Float and Shipboard Oxygen Observations at Depth Imparts Bias on Float pH and
750 Derived pCO₂. *Global Biogeochemical Cycles* 39, e2024GB008185.
751 <https://doi.org/10.1029/2024GB008185>

752 Chen, X., Qiu, B., Du, Y., Chen, S., & Qi, Y. (2016). Interannual and interdecadal variability of the
753 North Equatorial Countercurrent in the Western Pacific. *Journal of Geophysical Research: Oceans*,
754 121(10), 7743–7758. <https://doi.org/10.1002/2016JC012190>

755 Claustre, H., Johnson, K. S., & Takeshita, Y. (2020). Observing the Global Ocean with
756 Biogeochemical-Argo. *Annual Review of Marine Science*, 12(Volume 12, 2020), 23–48.
757 <https://doi.org/10.1146/annurev-marine-010419-010956>

758 D’Asaro, E. A., & McNeil, C. (2013). Calibration and Stability of Oxygen Sensors on Autonomous
759 Floats. <https://doi.org/10.1175/JTECH-D-12-00222.1>

760 Drucker, R., & Riser, S. C. (2016). In situ phase-domain calibration of oxygen Optodes on profiling
761 floats. *Methods in Oceanography*, 17, 296–318. <https://doi.org/10.1016/j.mio.2016.09.007>

762 Estapa, M. L., Feen, M. L., & Breves, E. (2019). Direct Observations of Biological Carbon Export
763 From Profiling Floats in the Subtropical North Atlantic. *Global Biogeochemical Cycles*, 33(3), 282–
764 300. <https://doi.org/10.1029/2018GB006098>

765 Giglio, D., Lyubchich, V., & Mazloff, M. R. (2018). Estimating Oxygen in the Southern Ocean Using
766 Argo Temperature and Salinity. *Journal of Geophysical Research: Oceans*, 123(6), 4280–4297.
767 <https://doi.org/10.1029/2017JC013404>

768 Helm, K. P., Bindoff, N. L., & Church, J. A. (2011). Observed decreases in oxygen content of the
769 global ocean. *Geophysical Research Letters*, 38(23). <https://doi.org/10.1029/2011GL049513>

770 Ito, T., Minobe, S., Long, M. C., & Deutsch, C. (2017). Upper ocean O₂ trends: 1958–2015.
771 *Geophysical Research Letters*, 44(9), 4214–4223. <https://doi.org/10.1002/2017GL073613>

772 Ito, T., Cervania, A., Cross, K., Ainchwar, S., & Delawalla, S. (2024). Mapping Dissolved Oxygen
773 Concentrations by Combining Shipboard and Argo Observations Using Machine Learning Algorithms.
774 *Journal of Geophysical Research: Machine Learning and Computation*, 1(3), e2024JH000272.
775 <https://doi.org/10.1029/2024JH000272>

776 Johnson, K. S., Plant, J. N., Riser, S. C., & Gilbert, D. (2015). Air Oxygen Calibration of Oxygen
777 Optodes on a Profiling Float Array. <https://doi.org/10.1175/JTECH-D-15-0101.1>

778 Johnson, K. S., Plant, J. N., Coletti, L. J., Jannasch, H. W., Sakamoto, C. M., Riser, S. C., et al. (2017).
779 Biogeochemical sensor performance in the SOCCOM profiling float array. *Journal of Geophysical*
780 *Research: Oceans*, 122(8), 6416–6436. <https://doi.org/10.1002/2017JC012838>

781 Johnson, K. S., & Bif, M. B. (2021). Constraint on net primary productivity of the global ocean by
782 Argo oxygen measurements. *Nature Geoscience*, 14(10), 769–774. [https://doi.org/10.1038/s41561-](https://doi.org/10.1038/s41561-021-00807-z)
783 [021-00807-z](https://doi.org/10.1038/s41561-021-00807-z)

784 Kalnay, E., Kanamitsu, M., Kistler, R., Collins, W., Deaven, D., Gandin, L., et al. (1996). The
785 NCEP/NCAR 40-Year Reanalysis Project. Retrieved from
786 [https://journals.ametsoc.org/view/journals/bams/77/3/1520-](https://journals.ametsoc.org/view/journals/bams/77/3/1520-0477_1996_077_0437_tnyrp_2_0_co_2.xml)
787 [0477_1996_077_0437_tnyrp_2_0_co_2.xml](https://journals.ametsoc.org/view/journals/bams/77/3/1520-0477_1996_077_0437_tnyrp_2_0_co_2.xml)

788 Kara, A. B., Rochford, P. A., & Hurlburt, H. E. (2000). An optimal definition for ocean mixed layer
789 depth. *Journal of Geophysical Research: Oceans*, 105(C7), 16803–16821.
790 <https://doi.org/10.1029/2000JC900072>

791 Keeling, R. F., Körtzinger, A., & Gruber, N. (2010). Ocean Deoxygenation in a Warming World.
792 *Annual Review of Marine Science*, 2 (Volume 2, 2010), 199–229.
793 <https://doi.org/10.1146/annurev.marine.010908.163855>

794 Kolodziejczyk, N., Portela, E., Thierry, V., & Prigent, A. (2024). ISASO2: recent trends and regional
795 patterns of ocean dissolved oxygen change. *Earth System Science Data*, 16(11), 5191–5206.
796 <https://doi.org/10.5194/essd-16-5191-2024>

797 Körtzinger, A., Schimanski, J., & Send, U. (2005). High Quality Oxygen Measurements from Profiling
798 Floats: A Promising New Technique. <https://doi.org/10.1175/JTECH1701.1>

799 Kwiatkowski, L., Torres, O., Bopp, L., Aumont, O., Chamberlain, M., Christian, J. R., et al. (2020).
800 Twenty-first century ocean warming, acidification, deoxygenation, and upper-ocean nutrient and
801 primary production decline from CMIP6 model projections. *Biogeosciences*, 17(13), 3439–3470.
802 <https://doi.org/10.5194/bg-17-3439-2020>

803 Lauvset, S. K., Lange, N., Tanhua, T., Bittig, H. C., Olsen, A., Kozyr, A., et al. (2022b).
804 GLODAPv2.2022: the latest version of the global interior ocean biogeochemical data product. *Earth
805 System Science Data*, 14(12), 5543–5572. <https://doi.org/10.5194/essd-14-5543-2022>

806 Li, C., Huang, Jianping, Ding, L., Liu, X., Yu, H., Huang, Jiping, 2020. Increasing Escape of Oxygen
807 From Oceans Under Climate Change. *Geophysical Research Letters* 47, e2019GL086345.
808 <https://doi.org/10.1029/2019GL086345>

809 Limburg, K. E., Breitburg, D., Swaney, D. P., & Jacinto, G. (2020). Ocean Deoxygenation: A Primer.
810 *One Earth*, 2(1), 24–29. <https://doi.org/10.1016/j.oneear.2020.01.001>

811 Masumoto, Y., Sasaki, H., Kagimoto, T., Komori, N., Ishida, A., Sasai, Y., et al. (2004). A fifty-year
812 eddy-resolving simulation of the world ocean: Preliminary outcomes of OFES (OGCM for the Earth
813 Simulator). *Journal of the Earth Simulator*, 1, 35–56. [https://www.jamstec.
814 go.jp/ceist/j/publication/journal/jes_vol.1/pdf/JES1-3.2-masumoto.pdf](https://www.jamstec.go.jp/ceist/j/publication/journal/jes_vol.1/pdf/JES1-3.2-masumoto.pdf)

815 Masumoto, Y. (2010). Sharing the results of a high-resolution ocean general circulation model under
816 a multi-discipline framework—a review of OFES activities. *Ocean Dynamics*, 60(3), 633–652.
817 <https://doi.org/10.1007/s10236-010-0297-z>

818 Maurer, T. L., Plant, J. N., & Johnson, K. S. (2021). Delayed-Mode Quality Control of Oxygen, Nitrate,
819 and pH Data on SOCCOM Biogeochemical Profiling Floats. *Frontiers in Marine Science*, 8.
820 <https://doi.org/10.3389/fmars.2021.683207>

821 Nakamura, T., & Awaji, T. (2004). Tidally induced diapycnal mixing in the Kuril Straits and its role
822 in water transformation and transport: A three-dimensional nonhydrostatic model experiment. *Journal*
823 *of Geophysical Research: Oceans*, 109(C9). <https://doi.org/10.1029/2003JC001850>

824 Nakamura, T., Awaji, T., Hatayama, T., Akitomo, K., Takizawa, T., Kono, T., et al. (2000a). The
825 Generation of Large-Amplitude Unsteady Lee Waves by Subinertial K1 Tidal Flow: A Possible
826 Vertical Mixing Mechanism in the Kuril Straits. Retrieved from
827 [https://journals.ametsoc.org/view/journals/phoc/30/7/1520-](https://journals.ametsoc.org/view/journals/phoc/30/7/1520-0485_2000_030_1601_tgolau_2.0.co_2.xml)
828 [0485_2000_030_1601_tgolau_2.0.co_2.xml](https://journals.ametsoc.org/view/journals/phoc/30/7/1520-0485_2000_030_1601_tgolau_2.0.co_2.xml)

829 Nakamura, T., Awaji, T., Hatayama, T., Akitomo, K., & Takizawa, T. (2000b). Tidal Exchange
830 through the Kuril Straits. Retrieved from [https://journals.ametsoc.org/view/journals/phoc/30/7/1520-](https://journals.ametsoc.org/view/journals/phoc/30/7/1520-0485_2000_030_1622_tetts_2.0.co_2.xml)
831 [0485_2000_030_1622_tetts_2.0.co_2.xml](https://journals.ametsoc.org/view/journals/phoc/30/7/1520-0485_2000_030_1622_tetts_2.0.co_2.xml)

832 Nicholson, D. P., & Feen, M. L. (2017). Air calibration of an oxygen optode on an underwater glider.
833 *Limnology and Oceanography: Methods*, 15(5), 495–502. <https://doi.org/10.1002/lom3.10177>

834 Ogata, T., & Nonaka, M. (2020). Mechanisms of Long-Term Variability and Recent Trend of Salinity
835 Along 137°E. *Journal of Geophysical Research: Oceans*, 125(2), e2019JC015290.
836 <https://doi.org/10.1029/2019JC015290>

837 Pacanowski, R. C., and S. M. Griffies (2000), MOM 3.0 Manual, Technical Report 4, 680 pp., Geophys.
838 Fluid Dyn. Lab., Princeton, N. J. Philander, S. G. H. (1990), El Niño, La Niña, and the Southern
839 Oscillation, pp. 293, Academic Press, San Diego, Calif.

840 Pörtner, H. O., & Farrell, A. P. (2008). Physiology and Climate Change. *Science*, 322(5902), 690–692.
841 <https://doi.org/10.1126/science.1163156>

842 Pozo Buil, M., & Di Lorenzo, E. (2017). Decadal dynamics and predictability of oxygen and
843 subsurface tracers in the California Current System. *Geophysical Research Letters*, 44(9), 4204–4213.
844 <https://doi.org/10.1002/2017GL072931>

845 Reid, J. L. (1997). On the total geostrophic circulation of the Pacific Ocean: flow patterns, tracers, and
846 transports. *Progress in Oceanography*, 39(4), 263–352. [https://doi.org/10.1016/S0079-
847 6611\(97\)00012-8](https://doi.org/10.1016/S0079-6611(97)00012-8)

848 Roemmich, D., & Gilson, J. (2009). The 2004–2008 mean and annual cycle of temperature, salinity,
849 and steric height in the global ocean from the Argo Program. *Progress in Oceanography*, 82(2), 81–
850 100. <https://doi.org/10.1016/j.pocean.2009.03.004>

851 Sampaio, E., Santos, C., Rosa, I. C., Ferreira, V., Pörtner, H.-O., Duarte, C. M., et al. (2021). Impacts
852 of hypoxic events surpass those of future ocean warming and acidification. *Nature Ecology &
853 Evolution*, 5(3), 311–321. <https://doi.org/10.1038/s41559-020-01370-3>

854 Sasaki, H., Nonaka, M., Masumoto, Y., Sasai, Y., Uehara, H., & Sakuma, H. (2008). An Eddy-
855 Resolving Hindcast Simulation of the Quasiglobal Ocean from 1950 to 2003 on the Earth Simulator.
856 In K. Hamilton & W. Ohfuchi (Eds.), *High Resolution Numerical Modelling of the Atmosphere and
857 Ocean* (pp. 157–185). New York, NY: Springer. https://doi.org/10.1007/978-0-387-49791-4_10

858 Sasano, D., Takatani, Y., Kosugi, N., Nakano, T., Midorikawa, T., & Ishii, M. (2015). Multidecadal
859 trends of oxygen and their controlling factors in the western North Pacific. *Global Biogeochemical
860 Cycles*, 29(7), 935–956. <https://doi.org/10.1002/2014GB005065>

861 Sasano, D., Takatani, Y., Kosugi, N., Nakano, T., Midorikawa, T., & Ishii, M. (2018). Decline and
862 Bidecadal Oscillations of Dissolved Oxygen in the Oyashio Region and Their Propagation to the
863 Western North Pacific. *Global Biogeochemical Cycles*, 32(6), 909–931.
864 <https://doi.org/10.1029/2017GB005876>

865 Schmidtko, S., Stramma, L., & Visbeck, M. (2017). Decline in global oceanic oxygen content during
866 the past five decades. *Nature*, 542(7641), 335–339. <https://doi.org/10.1038/nature21399>

867 Sharp, J. D., Fassbender, A. J., Carter, B. R., Johnson, G. C., Schultz, C., Dunne, J. P. (2022). GOBAI-
868 O₂: A Global Gridded Monthly Dataset of Ocean Interior Dissolved Oxygen Concentrations Based on
869 Shipboard and Autonomous Observations (NCEI Accession 0259304). NOAA National Centers for
870 Environmental Information. Dataset. <https://doi.org/10.25921/z72m-yz67>.

871 Sharp, J. D., Fassbender, A. J., Carter, B. R., Johnson, G. C., Schultz, C., & Dunne, J. P. (2023).
872 GOBAI-O₂: temporally and spatially resolved fields of ocean interior dissolved oxygen over nearly 2
873 decades. *Earth System Science Data*, 15(10), 4481–4518. <https://doi.org/10.5194/essd-15-4481-2023>

874 Stramma, L., Johnson, G. C., Sprintall, J., & Mohrholz, V. (2008). Expanding Oxygen-Minimum
875 Zones in the Tropical Oceans. *Science*, 320(5876), 655–658.
876 <https://doi.org/10.1126/science.1153847>

877 Stramma, L., Schmidtko, S., Bograd, S. J., Ono, T., Ross, T., Sasano, D., & Whitney, F. A. (2020).
878 Trends and decadal oscillations of oxygen and nutrients at 50 to 300 m depth in the equatorial
879 and North Pacific. *Biogeosciences*, 17(3), 813–831. <https://doi.org/10.5194/bg-17-813-2020>

880 Stramma, L., & Schmidtko, S. (2021). Tropical deoxygenation sites revisited to investigate oxygen
881 and nutrient trends. *Ocean Science*, 17(3), 833–847. <https://doi.org/10.5194/os-17-833-2021>

882 Suga, T., Takei, Y., & Hanawa, K. (1997). Thermostad Distribution in the North Pacific Subtropical
883 Gyre: The Central Mode Water and the Subtropical Mode Water. Retrieved from
884 [https://journals.ametsoc.org/view/journals/phoc/27/1/1520-
885 0485_1997_027_0140_tditnp_2.0.co_2.xml](https://journals.ametsoc.org/view/journals/phoc/27/1/1520-0485_1997_027_0140_tditnp_2.0.co_2.xml)

886 Suga, T., Motoki, K., Aoki, Y., & Macdonald, A. M. (2004). The North Pacific Climatology of Winter
887 Mixed Layer and Mode Waters. Retrieved from
888 [https://journals.ametsoc.org/view/journals/phoc/34/1/1520-
889 0485_2004_034_0003_tnpcow_2.0.co_2.xml](https://journals.ametsoc.org/view/journals/phoc/34/1/1520-0485_2004_034_0003_tnpcow_2.0.co_2.xml)

890 Takatani, Y., Sasano, D., Nakano, T., Midorikawa, T., & Ishii, M. (2012). Decrease of dissolved
891 oxygen after the mid-1980s in the western North Pacific subtropical gyre along the 137°E repeat
892 section. *Global Biogeochemical Cycles*, 26(2). <https://doi.org/10.1029/2011GB004227>

893 Takeshita, Y., Martz, T. R., Johnson, K. S., Plant, J. N., Gilbert, D., Riser, S. C., et al. (2013). A
894 climatology-based quality control procedure for profiling float oxygen data. *Journal of Geophysical*
895 *Research: Oceans*, 118(10), 5640–5650. <https://doi.org/10.1002/jgrc.20399>

896 Udaya Bhaskar, T. V. S., Sarma, V. V. S. S., & Pavan Kumar, J. (2021). Potential Mechanisms
897 Responsible for Spatial Variability in Intensity and Thickness of Oxygen Minimum Zone in the Bay
898 of Bengal. *Journal of Geophysical Research: Biogeosciences*, 126(6), e2021JG006341.
899 <https://doi.org/10.1029/2021JG006341>

900 Winkler, L. W. (1888). Die Bestimmung des im Wasser gelösten Sauerstoffes. *Berichte Der Deutschen*
901 *Chemischen Gesellschaft*, 21(2), 2843–2854. <https://doi.org/10.1002/cber.188802102122>

902 Wolf, M. K., Hamme, R. C., Gilbert, D., Yashayaev, I., & Thierry, V. (2018). Oxygen Saturation
903 Surrounding Deep Water Formation Events in the Labrador Sea From Argo-O₂ Data. *Global*
904 *Biogeochemical Cycles*, 32(4), 635–653. <https://doi.org/10.1002/2017GB005829>

905 Yasuda, I. (2004). North Pacific Intermediate Water: Progress in SAGE (SubArctic Gyre Experiment)
906 and Related Projects. *Journal of Oceanography*, 60(2), 385–395.
907 <https://doi.org/10.1023/B:JOCE.0000038344.25081.42>

908 You, Y. (2003). The pathway and circulation of North Pacific Intermediate Water. *Geophysical*
909 *Research Letters*, 30(24). <https://doi.org/10.1029/2003GL018561>

910

911

912